Tellus SERIES B CHEMICAL AND PHYSICAL METEOROLOGY
PUBLISHED BY THE INTERNATIONAL METEOROLOGICAL INSTITUTE IN STOCKHOLM

Tellus (2008), 60B, 685–705
Printed in Singapore. All rights reserved

TELLUS

Interannual variability in oceanic biogeochemical processes inferred by inversion of atmospheric O_2/N_2 and CO_2 data

By C. RÖDENBECK[1]*, C. LE QUÉRÉ[1]†, M. HEIMANN[1] and R. F. KEELING[2], [1]*Max Planck Institute for Biogeochemistry, P.O. Box 10 01 64, D-07701 Jena, Germany;* [2]*Scripps Institution of Oceanography, University of California, San Diego, California, USA*

(Manuscript received 21 December 2007; in final form 11 August 2008)

ABSTRACT

Atmospheric measurements of O_2/N_2 and CO_2 at up to nine sites have been used to infer the interannual variations in oceanic O_2 exchange with an inverse method. The method distinguishes the regional contributions of three latitudinal bands, partly the individual contributions of the North Pacific and the North Atlantic also. The interannual variations of the inferred O_2 fluxes in the tropical band correlate significantly with the El Niño/Southern Oscillation. Tropical O_2 variations appear to be dominated by the ventilation of the O_2 minimum zone from variations in Pacific equatorial upwelling. The interannual variations of the northern and southern extratropical bands are of similar amplitude, though the attribution to mechanisms is less clear. The interannual variations estimated by the inverse method are larger than those estimated by the current generation of global ocean biogeochemistry models, especially in the North Atlantic, suggesting that the representation of biological processes plays a role. The comparison further suggests that O_2 variability is a more stringent test to validate models than CO_2 variability, because the processes driving O_2 variability combine in the same direction and amplify the underlying climatic signal.

1. Introduction

Atmospheric carbon dioxide (CO_2) is rising at a rate controlled by the emissions from fossil-fuel burning and by CO_2 exchanges with the land and oceans. The oceans comprise a strong net sink, expected to further grow with the atmospheric CO_2 increase. The magnitude of oceanic CO_2 uptake in the future, however, is subject to feedbacks from changing climate. At present, such climate feedbacks are only poorly understood. Insight may be gained from investigating the response of ocean biogeochemistry to shorter-term natural variations, such as El Niño/Southern Oscillation (ENSO), Northern Annual Mode (NAM) or Southern Annual Mode (SAM). In principle, atmospheric CO_2 concentration measurements could reveal the signatures of these shorter-term variations in the oceanic CO_2 exchange. However, land processes entail atmospheric CO_2 variability on the same timescales but with higher amplitudes, so that conclusions about the ocean exchange are generally difficult.

The variations in atmospheric CO_2 are associated with variations in atmospheric O_2. Most biogeochemical processes—photosynthesis, autotrophic or heterotrophic respiration, burning of biomass or fossil fuels—release or consume CO_2 and O_2 in specific stoichiometric ratios. On land, CO_2 and O_2 exchanges with the atmosphere directly reflect these stochiometries. In contrast, ocean–atmosphere exchanges of CO_2 and O_2 are partly decoupled from each other: the buffer effect of the carbonate chemistry leads to much slower equilibration rates of CO_2 compared with O_2. Further, upwelling brings deep water of various CO_2:O_2 ratios to the surface. Finally, warming/cooling leads to outgassing/uptake of both CO_2 and O_2 due to solubility changes, that is, exchange of the same rather than the opposite direction for the two gases. Quantification of O_2 fluxes in addition to that of CO_2 therefore gives independent information to disentangle these oceanic processes.

The atmospheric O_2 concentration has been measured regularly at remote sites for more than 15 years, with the principle goal of constraining long-term carbon budgets (Langenfelds et al., 1999; Bender et al., 2005; Tohjima et al., 2003; Manning and Keeling, 2006). Measuring O_2 concentration at the required precision is demanding because the variations are small compared with the large background. The measurements show that the long-term CO_2 increase is accompanied by a long-term O_2

*Corresponding author.
e-mail: christian.roedenbeck@bgc-jena.mpg.de
†Now at: School of Environmental Sciences, University of East Anglia, Norwich, UK, and British Antarctic Survey, Cambridge, UK
DOI: 10.1111/j.1600-0889.2008.00375.x

decrease. These trends are useful for separating land and ocean contributions in the long-term global carbon sink (Keeling and Shertz, 1992). In addition, the atmospheric O_2 concentration exhibits seasonal cycles, as well as gradients with latitude, which provide useful constraints on ocean biological production, air–sea gas exchange and large-scale ocean transport (e.g. Stephens et al., 1998; Garcia and Keeling, 2001; Gruber et al., 2001; Battle et al., 2006; Nägler et al., 2007). The loss rate of O_2 also shows considerable variations year-to-year, as do the spatial gradients between stations. Such shorter-term interannual variability has received only little attention so far but could help to quantify the oceanic response to climate variations as outlined above.

An oceanic signal can be isolated from O_2 measurements by combining them with CO_2 measurements to compute the tracer 'atmospheric potential oxygen' (APO) introduced by Stephens et al. (1998). Atmospheric potential oxygen is effectively the O_2 concentration plus 1.1 times the CO_2 concentration, where 1.1 is the approximate average ratio of O_2 production/consumption to CO_2 consumption/production by terrestrial photosynthesis and respiration (Severinghaus, 1995). Any process with such a stoichiometry does not change APO, because the effect on CO_2 cancels the effect on O_2. Fossil-fuel burning consumes O_2 at a slightly higher ratio due to hydrogen oxidation and therefore decreases APO, but this effect can be accounted for, based on fossil-fuel use statistics. Fossil-fuel corrected APO effectively responds to oceanic exchange only.

Understanding the origin of APO variations is complicated because they are caused by sea–air fluxes of both O_2 and CO_2 (as atmospheric abundances of oxygen are measured in terms of O_2/N_2 ratios, there is also a small influence from N_2 fluxes). On seasonal and interannual timescales, the sea–air O_2 exchange is expected to dominate the APO variations due to the dampening of CO_2 exchange by the buffering chemistry (Keeling and Severinghaus, 2000). Importantly, however, all of the oceanic processes that drive changes in APO (warming/cooling, biological production, gas exchange) are also important for driving exchanges of CO_2. Atmospheric potential oxygen measurements can therefore be used to challenge our understanding of the processes relevant for CO_2.

To interpret atmospheric measurements in terms of surface fluxes, atmospheric transport needs to be taken into account. We use a tracer transport model that simulates the atmospheric tracer concentration at the stations in response to surface–air tracer exchange. This exchange is then estimated using inverse methods, determining those fluxes that result in the best match between modelled and observed concentrations. This 'atmospheric transport inversion' is a well-established tool to quantify sources and sinks of CO_2 (or other gases) and their spatial and temporal variations (e.g. Rayner et al., 1999; Bousquet et al., 2000; Gurney et al., 2002; Rödenbeck et al., 2003; Baker et al., 2006). This technique can also be applied to APO to yield estimates of the surface 'APO flux', which can be defined as a combination of O_2, CO_2 and N_2 fluxes. In contrast to CO_2 which is presently observed at over 100 sites, however, there is only a small number of sites where multi-year APO records exist so far. On the other hand, the limitation of a sparse atmospheric network is counteracted by the important advantage of APO that its terrestrial fluxes can be assumed to vanish, so that only oceanic fluxes need to be adjusted.

This paper explores the suitability of such an APO inversion to gain information about interannual ocean variability. In this preliminary study, we focus on data from the Scripps O_2 program, as more research is needed before results from multiple programmes can be combined in this context. We describe the mathematical setup used to estimate APO fluxes from atmospheric observations, including the specification of data, models and a-priori assumptions. We present spatial and temporal variations of the resulting APO fluxes and some measures of their uncertainty. Implications of these APO flux estimates for the strength of interannual variations in different latitude bands of the ocean, and for their relation to climate variability are discussed. In a companion paper, Hamme and Keeling (2008) discuss interannual variations in APO data with respect to variations in ocean ventilation and other possible driving mechanisms.

2. Inversion method

2.1. Formalism

We estimate APO fluxes using a global atmospheric transport inversion, methodologically similar to previous studies of CO_2 (in particular, to Rödenbeck et al., 2003 and its extensions described in Rödenbeck, 2005). The primary input is the observed concentrations. The entire set of measured values at different times and locations is denoted by the vector $\mathbf{c}_{\mathrm{obs}}$ (Section 2.2). An atmospheric tracer transport model (Section 2.3) calculates modelled concentrations $\mathbf{c}_{\mathrm{mod}}$ that arise from a temporally and spatially varying flux field $\mathbf{f}$. The values in $\mathbf{c}_{\mathrm{mod}}$ are sampled in the model for every individual time and location where there is a measured value in $\mathbf{c}_{\mathrm{obs}}$. The concentration of a conserved, passive tracer (i.e. one that doesn't influence the transport and is sufficiently unreactive) can be linearly related to the fluxes according to

$$\mathbf{c}_{\mathrm{mod}} = \mathbf{A}\mathbf{f} + \mathbf{c}_{\mathrm{ini}}, \tag{1}$$

with the transport matrix $\mathbf{A}$ and the initial concentration $\mathbf{c}_{\mathrm{ini}}$. The inversion calculation seeks those fluxes $\mathbf{f}$ that lead to the best match between observed and modelled concentrations, in the sense that the value of the cost function

$$J_{\mathbf{c}} = \frac{1}{2}(\mathbf{c}_{\mathrm{obs}} - \mathbf{c}_{\mathrm{mod}})^{\mathrm{T}}\mathbf{Q}_{\mathbf{c}}^{-1}(\mathbf{c}_{\mathrm{obs}} - \mathbf{c}_{\mathrm{mod}}) \tag{2}$$

is minimal. The (diagonal) matrix $\mathbf{Q}_{\mathbf{c}}$ introduces a weighting among the concentration values, involving assumed measurement uncertainty, location-dependent model uncertainty, and a data density weighting (see Appendix B1 for details).

Table 1. Codes, names, locations and model uncertainty classes (see Appendix B1) of the sites measuring O_2 and CO_2 concentrations that were used in the inversion.

Station code	Name	Latitude (°)	Longitude (°)	Height (m a.s.l.)	Mod. Unct. Class
ALT	Alert, Canada	82.45	−62.52	210	S
CBA	Cold Bay, Alaska	55.20	−162.72	25	S
CGO	Cape Grim, Tasmania	−40.68	144.68	94	S
KUM	Cape Kumukahi, Hawaii	19.52	−154.82	40	R
LJO	La Jolla, USA	32.87	−117.25	15	S
MLO	Mauna Loa, Hawaii	19.53	−155.58	3397	R
PSA	Palmer Station, Antarctica	−64.92	−64.00	10	R
SMO	Tutuila, Am. Samoa, Pacific	−14.25	−170.57	42	R
SPO	South Pole	−89.98	−24.80	2810	R

However, the data density from discrete surface stations is too low to reliably determine the large number of degrees of freedom represented by the vector **f** (flux values at all the grid cells of the transport model every day), that is, minimization of the above cost function with respect to the fluxes would be an ill-posed problem. As a remedy, additional information is supplied, based on measurement-derived data sets as well as on statistical assumptions about APO fluxes. This is done here by writing the flux field **f** in terms of a set of dimensionless adjustable parameters (vector **p**) as

$$\begin{aligned}\mathbf{f}(\mathbf{p}) &= \mathbf{f}_{\text{fix}} + \mathbf{f}_{\text{adj}}(\mathbf{p}).\\ &= \mathbf{f}_{\text{fix}} + \mathbf{F}\mathbf{p}\end{aligned} \tag{3}$$

This relation represents a simple linear statistical flux model, to be detailed in Section 2.4 below. In short, each of the adjustable parameters in **p** acts as a multiplier to one of the columns of the matrix **F**. These columns represent elementary spatio-temporal flux patterns (like elementary flux pulses) composing the total flux. They incorporate both an assumed spatio-temporal weighting of the surface flux (e.g. determining areas of large versus small expected flux variability) and its spatial and temporal coherence (e.g. determining expected characteristic length and timescales of flux variability). In addition, a fixed flux field $\mathbf{f}_{\text{fix}}$ is split off from the adjustable component. It accounts for flux contributions considered better constrained from external information than from the expected atmospheric information (e.g. contributions due to fossil-fuel burning). Mathematical stability of the flux estimation is ensured by adding a second term to the cost function,

$$J = J_{\text{c}} + \frac{1}{2}\mathbf{p}^{\text{T}}\mathbf{p}, \tag{4}$$

which 'penalizes' larger deviation of the parameters from zero. This augmented cost function J follows from usual Bayesian estimation theory and corresponds to introduction of an a-priori probability distribution with best-guess $\langle \mathbf{f} \rangle_{\text{pri}} = \mathbf{f}_{\text{fix}}$ and an implied covariance matrix[1] $\mathbf{Q}_{\mathbf{f},\text{pri}} = \mathbf{F}\mathbf{F}^{\text{T}}$. The flux model can also be viewed as a stabilizing 'preconditioner' because the number of degrees of freedom is now the number of parameters, chosen to be as small as possible.

The minimization of the cost function J with respect to the parameters **p** has been done using a Conjugate Gradients algorithm with re-orthogonalization after each step (Rödenbeck, 2005).

2.2. Atmospheric data

The inversions performed here focus on O_2 and CO_2 data from the programme of R. F. Keeling at the Scripps Institution of Oceanography, which includes data from flasks collected at the sites listed in Table 1. We used data from the archive version of 28 June 2006 (cf. Hamme and Keeling, 2008). Flask values are screened based on agreement with replicates and other known analytical or sampling artefacts. Each data point used in the calculation reflects the average of the retained flask replicates (typically three in number) collected at a given date and station.

Sampling at the different stations began at different times, so the Scripps data set is not homogeneous with time. The sudden appearance of a new station can lead to spurious flux variations in inversion calculations.[2] To eliminate this problem, we have grouped the sites into differently large sets based on record length (Fig. 1). In any figures or statistical computation below,

[1] Traditionally, a-priori uncertainties and correlations are specified through the a-priori flux covariance matrix $\mathbf{Q}_{f,\text{pri}}$ in a cost function, written in terms of fluxes. Here, a-priori uncertainties and correlations are specified 'implicitly' through the matrix **F**, to gain more flexibility and transparency in the definition of the a-priori constraints. The implied flux covariance matrix $\mathbf{Q}_{\mathbf{f},\text{pri}} = \mathbf{F}\mathbf{F}^{\text{T}}$ itself is not used anywhere in the calculation (Rödenbeck, 2005).

[2] Such jumps can arise as the region of influence of a site changes from prior-constrained to data-constrained, with generally different mean values. Though this transition would potentially be detectable from an accompanying decrease in the a-posteriori uncertainty, the resulting time-series would be hard to interpret.

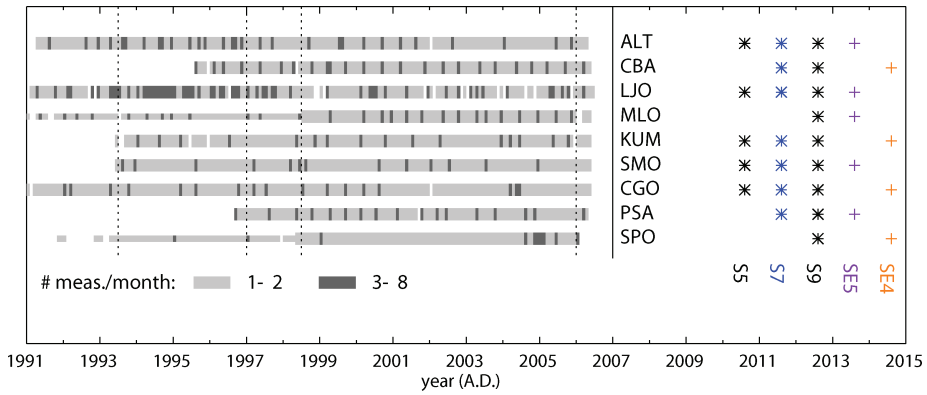

Fig. 1. Left-hand panel: Data availability for each site, shown as number of measurement instants per month. Sites are ordered according to latitude. For MLO and SPO, the narrow bands indicate data that have been excluded. Right-hand panel: Membership of the sites in the various sets. The colours correspond to the results' figures.

the flux results will be truncated to the respective time periods, where the records of all involved sites actually contain data (see vertical lines in Fig. 1). The main runs were done using sets S5, S7 or S9.

For MLO (Mauna Loa, Hawaii) and SPO (South Pole, Antarctica), Manning and Keeling (2006) document sampling problems for all data before mid 1998 (though the seasonality may still be well represented). Therefore, results using these two sites are only considered after mid 1998.

2.3. Transport model

Atmospheric transport (matrix **A**) is calculated by the global offline atmospheric transport model TM3 (Heimann and Körner, 2003) with different spatial resolutions (Table 2). The model is driven by 6-hourly meteorological fields derived from the NCEP reanalysis (Kalnay et al., 1996) that covers all our target period in a consistent manner. The meteorological input varies interannually according to the true year of simulation. Modelled concentration values are picked from the model grid box that contains the respective site (in the case of MLO, an elevated model level is sampled to account of the mountain location not represented in the model topography). Each modelled value is taken at the same date and time at which the corresponding measured value has been sampled. The initial concentration $\mathbf{c}_{\mathrm{ini}}$ represents a well-mixed atmosphere with a fixed APO mixing ratio (Appendix B2).

2.4. The flux model ('a-priori information')

In specifying the 'flux model' (i.e. **F** and $\mathbf{f}_{\mathrm{fix}}$ of eq. 3), we have tried to only include just as much detail as necessary to ensure that the inversion is well-posed mathematically. In particular, we avoided almost any explicit time dependence on interannual scale in these constraints, in order that all temporal features of the estimated APO flux can be traced to atmospheric information.

Table 2. Summary of alternative choices taken in the various inversion runs. The unlabelled choice in each category represents the standard

Label	Description
	Data
	Station set S5
S7	Station set S7
S9	Station set S9
S5sm	Station set S5, global mean subtr. from data
S5a=1	Station set S5, stoichiometry $\alpha = 1.0$
	Inversion setup
	Standard setup as of Section 2.4
loose priors	A priori *SD* increased by factor 2
tight priors	A priori *SD* decreased by factor 2
long corr.	A priori correlation length incr. by factor 2
high freq.	A priori correlation time decreased by factor 2
	Transport model resolution
	$\approx 8^\circ$ lat. $\times 10^\circ$ long. $\times$ 9 vert. levels
fg	$\approx 4^\circ$ lat. $\times 5^\circ$ long. $\times$ 19 vert. levels
	Transport model drivers
	Meteorology of actual years
1990 winds	Repeated 1990 meteorology
1995 winds	Repeated 1995 meteorology
1997 winds	Repeated 1997 meteorology

2.4.1. Flux components and processes. To a very good approximation (Appendix A), the APO flux can be written as

$$\mathbf{f}^{\mathrm{APO}} = \mathbf{f}^{\mathrm{O_2}} + 1.1\mathbf{f}^{\mathrm{CO_2}} - \frac{X_0^{\mathrm{O_2}}}{X_0^{\mathrm{N_2}}}\mathbf{f}^{\mathrm{N_2}}, \tag{5}$$

where $X_0^{\mathrm{O_2}}$ and $X_0^{\mathrm{N_2}}$ denote reference mixing ratios of O_2 and N_2. The APO flux can further be expanded into different contributing processes:

$$\begin{aligned}\mathbf{f}^{\mathrm{APO}} = &\left(\mathbf{f}^{\mathrm{O_2,oc}} + 1.1\mathbf{f}^{\mathrm{CO_2,oc}} - \frac{X_0^{\mathrm{O_2}}}{X_0^{\mathrm{N_2}}}\mathbf{f}^{\mathrm{N_2,oc}}\right),\\ &+(\mathbf{f}^{\mathrm{O_2,ff}} + 1.1\mathbf{f}^{\mathrm{CO_2,ff}})\end{aligned} \tag{6}$$

where superscript 'oc' refers to oceanic processes and 'ff' to fossil-fuel burning or other anthropogenic processes. By construction of APO, any contribution from the land biosphere ($\mathbf{f}^{\mathrm{APO,lbio}} = \mathbf{f}^{\mathrm{O_2,lbio}} + 1.1\ \mathbf{f}^{\mathrm{CO_2,lbio}}$) is cancelling out to the extent that the stoichiometric ratio is $\mathbf{f}^{\mathrm{O_2,lbio}} = -1.1\ \mathbf{f}^{\mathrm{CO_2,lbio}}$. N_2 fluxes $\mathbf{f}^{\mathrm{N_2,lbio}}$ from nitrogen fixation or denitrification have been neglected, assuming that they are much smaller than the oceanic fluxes $\mathbf{f}^{\mathrm{N_2,oc}}$ driven by solubility changes from warming and cooling.

Each of the APO flux contributions in the right-hand side (r.h.s.) of eq. (6) can be further split into its respective contributions to the fixed and the adjustable terms of the flux model eq. (3). Part of the oceanic contributions, as well as all the fossil-fuel contributions, are split off to form the fixed term,

$$\mathbf{f}_{\mathrm{fix}}^{\mathrm{APO}} = \left(\mathbf{f}_{\mathrm{fix}}^{\mathrm{O_2,oc}} + 1.1\,\mathbf{f}_{\mathrm{fix}}^{\mathrm{CO_2,oc}} - \frac{X_0^{\mathrm{O_2}}}{X_0^{\mathrm{N_2}}}\,\mathbf{f}_{\mathrm{fix}}^{\mathrm{N_2,oc}}\right) + \left(\mathbf{f}_{\mathrm{fix}}^{\mathrm{O_2,ff}} + 1.1\,\mathbf{f}_{\mathrm{fix}}^{\mathrm{CO_2,ff}}\right). \tag{7}$$

Consequently, the adjustable term only has oceanic contributions,

$$\mathbf{f}_{\mathrm{adj}}^{\mathrm{APO}} = \left(\mathbf{f}_{\mathrm{adj}}^{\mathrm{O_2,oc}} + 1.1\,\mathbf{f}_{\mathrm{adj}}^{\mathrm{CO_2,oc}} - \frac{X_0^{\mathrm{O_2}}}{X_0^{\mathrm{N_2}}}\,\mathbf{f}_{\mathrm{adj}}^{\mathrm{N_2,oc}}\right). \tag{8}$$

2.4.2. Specification of the fixed terms. The following data sets have been chosen to form the fixed APO flux $\mathbf{f}_{\mathrm{fix}}^{\mathrm{APO}}$ of eq. (7):

The contribution from sea–air oxygen fluxes ($\mathbf{f}_{\mathrm{fix}}^{\mathrm{O_2,oc}}$) has been taken from the results of the ocean transport inversion, based on ocean interior data by Gruber et al. (2001), smoothed in space. It is constant in time.

The contribution from sea–air CO_2 fluxes ($\mathbf{f}_{\mathrm{fix}}^{\mathrm{CO_2,oc}}$) represents a climatological seasonal cycle. The long-term mean is taken from the ocean inversion by Gloor et al. (2003), smoothed in space. The seasonal and fine-scale spatial patterns are taken from the ΔpCO_2-based estimates by Takahashi et al. (2002) (cf. Fig. 13).

Sea–air nitrogen fluxes arise from temperature-induced solubility changes in the ocean. A contribution to the fixed term has been calculated from NCEP heat fluxes (Kalnay et al., 1996), using the temperature and salinity dependent formula by Weiss (1970). We use a climatological nitrogen correction $\mathrm{f}_{\mathrm{fix}}^{\mathrm{N_2,oc}}$ without interannual variations (compare Fig. 13).

CO_2 emissions from fossil-fuel burning and cement manufacturing ($\mathbf{f}_{\mathrm{fix}}^{\mathrm{CO_2,ff}}$) are taken from energy consumption statistics (Olivier and Berdowski, 2001). The corresponding fossil-fuel O_2 flux is computed by scaling the CO_2 flux according to

$$\mathbf{f}_{\mathrm{fix}}^{\mathrm{O_2,ff}} = -1.4\,\mathbf{f}_{\mathrm{fix}}^{\mathrm{CO_2,ff}}. \tag{9}$$

The factor of -1.40 is supported by the estimates of the global emissions over various fuel types and cement (CDIAC) and fuel composition data from Keeling (1988). The global stoichiometry can vary due to changes in the mix of fuel burned but, in fact, was highly constant over the relevant period (range from 1.39 to 1.40). Our approach also neglects geographic variability in the fuel mix. The employed data set $\mathbf{f}_{\mathrm{fix}}^{\mathrm{CO_2,ff}}$ includes the slight changes from year to year, but any seasonal, weekly or diurnal variations of fossil-fuel emissions are neglected. The emissions are heterogeneous in space due to point-like sources.

2.4.3. Specification of the adjustable terms. The adjustable term $\mathbf{f}_{\mathrm{adj}} = \mathbf{Fp}$ is not implemented as an explicit sum of O_2, CO_2 and N_2 contributions, but rather expanded into timescales – long-term flux (superscript 'lt'), mean seasonality ('seas'), and non-seasonal variations ('var', interannual and high-frequency variations):

$$\mathbf{f}_{\mathrm{adj}}^{\mathrm{APO}} = \mathbf{f}_{\mathrm{adj}}^{\mathrm{APO,lt}} + \mathbf{f}_{\mathrm{adj}}^{\mathrm{APO,seas}} + \mathbf{f}_{\mathrm{adj}}^{\mathrm{APO,var}}. \tag{10}$$

Each contribution is of the form $\mathbf{f}_{\mathrm{adj}}^{i} = \mathbf{F}^{i}\,\mathbf{p}^{i}$ with i standing for 'lt', 'seas' or 'var', where the vectors $\mathbf{p}^{i}$ denote the respective subsets of parameters in $\mathbf{p}$ and the matrices $\mathbf{F}^{i}$ denote the corresponding groups of columns of $\mathbf{F}$. To further explain their construction, the vector notation $\mathbf{F}$, with vector elements referring to the grid cells and time steps of the model, is replaced by the field notation $f(x, y, t)$ highlighting the space and time dependence. Then, each of the three terms $\mathbf{f}_{\mathrm{adj}}^{i}$ has the structure

$$f_{\mathrm{adj}}^{i}(x, y, t) = f_{\mathrm{sh},i}(x, y) \sum_{m_{\mathrm{t}}=1}^{N_{\mathrm{t},i}} \sum_{m_{\mathrm{s}}=1}^{N_{\mathrm{s},i}} g_{m_{\mathrm{t}},i}^{\mathrm{time}}(t)\, g_{m_{\mathrm{s}},i}^{\mathrm{space}}(x, y)\, p_{m_{\mathrm{t}},m_{\mathrm{s}},i}. \tag{11}$$

Each column of $\mathbf{F}^{i}$ corresponds to one of the terms (m_{t}, m_{s}) of this sum, to be scaled during estimation by the adjustable parameter $p_{m_{\mathrm{t}},m_{\mathrm{s}},i}$. The sums run over a set of temporal elements $g_{m_{\mathrm{t}},i}^{\mathrm{time}}(t)$ and a set of spatial elements $g_{m_{\mathrm{s}},i}^{\mathrm{space}}(x, y)$, which represent decompositions of the inversion's time interval and the Earth's surface, respectively.

The temporal decomposition (sum over m_{t}) is a Fourier series, where $f_{\mathrm{adj}}^{\mathrm{seas}}$ only contains the seasonal Fourier components (those with frequencies 1/yr, 2/yr, etc.), $f_{\mathrm{adj}}^{\mathrm{var}}$ the non-seasonal Fourier components (all other frequencies, comprising interannual and short-term variations), and $f_{\mathrm{adj}}^{\mathrm{lt}}$ the (single) time-mean Fourier term. The individual Fourier terms are multiplied by spectral weights corresponding to a low-pass filter with an upper limit frequency of 12/yr (i.e. half-monthly, Fig. 4, upper panel). By the properties of the Fourier transformation, this is equivalent to a-priori temporal correlations on a timescale of the order of around two weeks. The choice of this frequency reflects, on the one hand, the fact that there is no information on higher frequencies in the mainly two-weekly flask data. On the other hand, we also expect temporal correlations due to the inertia of the oceanic processes and because gas exchange and upwelling are driven by the atmosphere on synoptic time-scales. As the real correlation timescales are not well known, the limit frequency will be varied in a sensitivity test ('high freq.', Table 2).

The spatial decomposition is a sum (over m_{s}) of small regional elements $g_{m_{\mathrm{s}},i}^{\mathrm{space}}(x, y)$, centred along a regular grid of pixels $\approx 8^{\circ}$ latitude $\times 10^{\circ}$ longitude in size (aggregates of 4 pixels of the

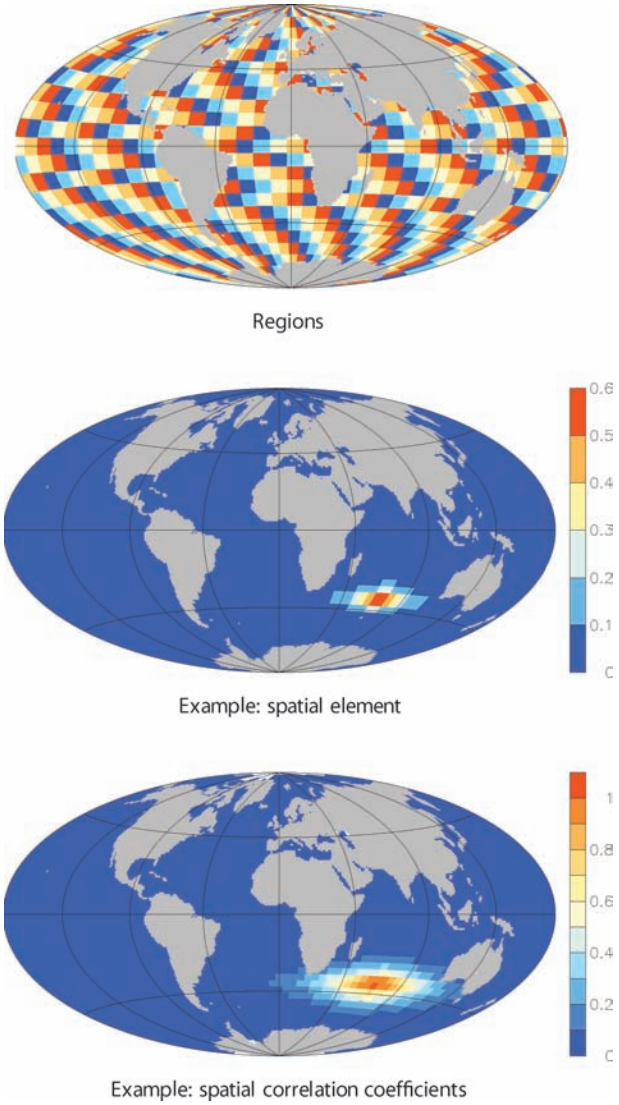

Fig. 2. Top panel: regular grid of regions used in the flux model: spatially, there is one parameter per such region.
Middle panel: Example of a spatial element $g^{\text{space}}_{m_s,i}(x, y)$ as in eq. (11).
Bottom panel: Implied spatial correlation coefficients with respect to an example location.

transport model, see Fig. 2, top panel). Each of these spatial elements overlaps its neighbours with exponentially decaying tails, as shown by the example element in Fig. 2, middle panel. Due to these tails, fluxes in adjacent locations are partially linked together, leading to a-priori correlations. The bottom panel shows the resulting correlation coefficients with respect to an example location. The chosen *e*-folding lengths (≈3200 km in longitude and ≈960 km in latitude) are largely arbitrary and will therefore be varied in a sensitivity test ('long corr.', Table 2). The spatial correlation structure is identical for non-seasonal, seasonal and constant terms.

Finally, the adjustable terms are, at each location (x, y) and each time t, proportional to the spatial weighting ('shape') $f_{\text{sh},i}(x, y)$. By construction, this 'shape' determines the a-priori standard deviation of the adjustable term at every point and instant (given suitable normalization of the spatial and temporal decompositions, Rödenbeck, 2005). As flux adjustments at any location/time are the more penalized the larger they are in units of their respective a-priori standard deviation, this weighting guides the inversion so that signals in the data will preferably lead to flux signals in areas where $f_{\text{sh},i}(x, y)$ is large. In that way, the 'shape' defines the domain of activity of the flux component. For all three timescales, the 'shape' is non-zero only over ice-free ocean areas:

(1) For the seasonal variations (term $\mathbf{f}^{\text{APO,seas}}_{\text{adj}}$), the 'shape' at any point equals the seasonal cycle amplitude (standard deviation) of the oxygen flux data set by Garcia and Keeling (2001) based on air–sea difference in partial pressure (smoothed in space), enhanced by an arbitrary factor of 3 meant to prevent undue damping of seasonality (Fig. 3, middle panel). The choice of the Garcia and Keeling (2001) data set reflects that APO flux seasonality is assumed to be dominated by O_2 and that a seasonal CO_2 and N_2 contribution is already contained in the fixed term $\mathbf{f}^{\text{APO}}_{\text{fix}}$.

(2) In contrast, for the non-seasonal variations (interannual and high-frequency, term $\mathbf{f}^{\text{APO,var}}_{\text{adj}}$), no such detailed expectations on the spatial distribution of variability amplitudes are available a-priori; therefore, the local standard deviation is simply set to a constant per-area value in all ice-free areas (Fig. 3, bottom panel). The value itself is determined from the normalization condition that the globally integrated and interannually filtered (as described in Section 2.5) flux component $\mathbf{f}^{\text{APO,var}}_{\text{adj}}$ has an a-priori standard deviation of 612 Tmol/yr at any time. This choice (corresponding to $f_{\text{sh,var}}(x, y) = 1\mu\text{mol m}^{-2}\text{s}^{-1}$ in the open ocean for the standard choices of the correlation parameters) is largely arbitrary and will therefore be varied in sensitivity tests ('loose priors' and 'tight priors', Table 2).

(3) The 'shape' of the long-term APO fluxes (constant term $\mathbf{f}^{\text{APO,lt}}_{\text{adj}}$) is proportional to that of the non-seasonal variations, but scaled such that $\mathbf{f}^{\text{APO,lt}}_{\text{adj}}$ is tighter (a-priori sigma of only 56%) than the constant Fourier term that would correspond to $\mathbf{f}^{\text{APO,var}}_{\text{adj}}$. Due to this tighter standard deviation, the long-term APO fluxes are more strongly determined by the data-based a-priori long-term values of Section 2.4.2, reflecting that atmospheric inversions are generally considered weak at estimating long-term fluxes and that our focus is on the interannual variations.

2.5. *Postprocessing: filtering and aggregation*

Although the numerical time resolution of the inversion is daily, the results are smooth on timescales shorter than around two weeks, due to the a-priori prescribed correlations. As we focus on interannual variations, however, we further filter the

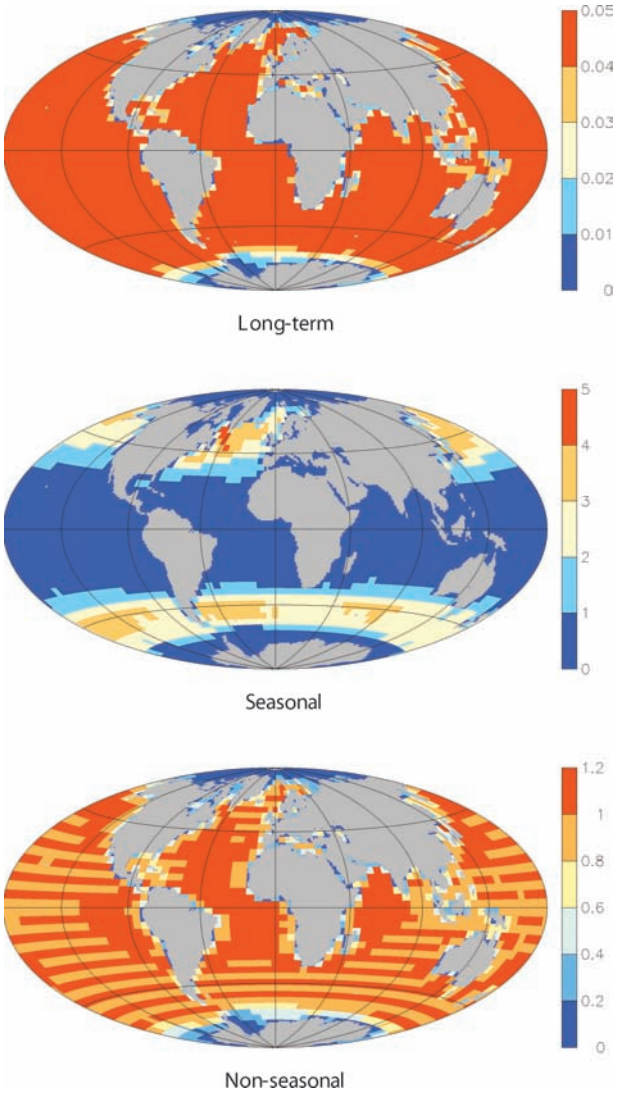

Fig. 3. Flux model: Spatial structure of the 'shapes' $\mathbf{f}_{sh,i}$ for the 3 considered timescales (μmol m^{-2} s^{-1}); (The stripe structure in some maps only results from insignificant numerical deviations in the normalization which are unavoidable due to the aggregated pixels.)

results by subtracting the mean seasonal cycle and most variations faster than 1 yr (Gaussian spectral weights, see 'Filt0.5gd' of Rödenbeck, 2005, Fig. 4, lower panel). This filter essentially retains annual averages.

Likewise, although the inversion numerically provides flux estimates on pixel resolution, the results are smooth at any scales smaller than a few 1000 km. For most of the analysis, however, we integrate the fluxes into three latitudinal bands (approx. 90°S–20°S, 20°S–20°N and 20°N–90°N). This takes into account the actual spatial resolution of the atmospheric information, determined by the distance between the atmospheric sites, as suggested by a resolution analysis (next section).

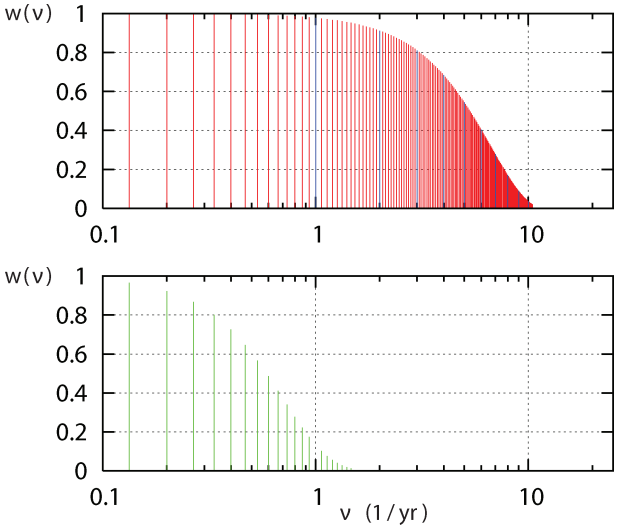

Fig. 4. Upper panel: relative spectral weights used to define the temporal a-priori correlations in the adjustable terms (standard setup, blue—seasonal component, red—non-seasonal component). Lower panel: relative spectral weights of the interannual filter used in the post-processing of the inversion results.

2.6. *Testing the method*

As a consistency check, the flux estimates from the inversion have been used as input to a run of our transport model (i.e. they have been substituted into eq. 1). The thus modelled concentrations should closely match the data (formally within the uncertainty bounds specified in $\mathbf{Q}_c$). The outcome will be discussed later in Section 3.2.1 (Fig. 7).

To test the suitability of the algorithm for estimating interannual APO variations, we assessed how well a given APO flux field can be reproduced by the inversion algorithm from pseudo-data, created by a forward transport model run of those fluxes. As described in Appendix C, these synthetic inversions establish that seasonality and interannual variations of the fluxes can be reconstructed in at least the three latitudinal bands used for post-aggregation.

A further test is provided by comparison of APO flux variations with independent data-based estimates. Appendix D confirms good phase agreement between APO flux seasonality estimated by the inversion and that from oxygen partial pressure differences.

3. Results

3.1. *Estimated interannual variability of APO fluxes*

Interannually filtered time-series of estimated APO fluxes for the global ocean and for each of the three latitude bands are shown in Fig. 5. The different lines correspond to runs based on the measurements of station sets S5, S7 and S9 of Fig. 1, using the standard setup as described in Section 2. The longest line

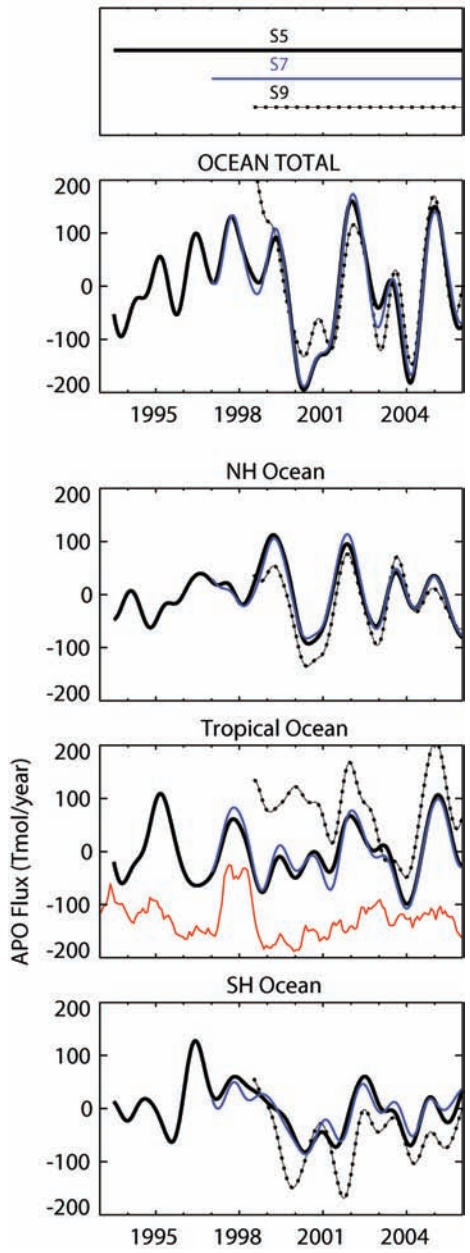

Fig. 5. Interannual variations of APO fluxes retrieved from the atmospheric data (5, 7 or 9 sites, standard setup). APO fluxes have been integrated over the total ocean (top) and over three latitude bands (approx. 90°S–20°S, 20°S–20°N, 20°N–90°N). Time-series are deseasonalized and filtered for interannual variability (as in Rödenbeck, 2005), and the mean (1993–2005) has been subtracted (anomalies only; positive values denote an increased source into the atmosphere). Tropical fluxes are shown with a monthly ENSO index (MEI) over-plotted in red.

(using S5 and the standard setup) will be referred to as the 'base run'.

Figure 6 gives statistical properties of the base run over the period 1993–2005. It also shows statistical properties of many additional runs explained further below. We draw attention to the following features in the base run (wide black bars or dots on the far left-hand side in each group of bars):

(1) Estimated interannual variability (IAV) in the global APO flux is around ± 90 Tmol yr^{-1} (standard deviation), in good agreement with the variations computed directly from the atmospheric observations (Hamme and Keeling, 2008).

(2) The three latitudinal bands show variations of similar amplitude (around ± 50 Tmol yr^{-1} each).

(3) Tropical fluxes tend to show positive anomalies during El Niño periods (high El Niño index as given by the red line of Fig. 5) and, even more clearly, negative ones during La Niñas. The relation to ENSO is confirmed statistically by a moderate, but over 97% significant,[3] correlation between the Tropical variability and the MEI El Niño index (Fig. 6, panel B).

3.2. *Uncertainty*

Before discussing the implications of these findings, we first evaluate whether they are robust relative to various conceivable sources of error.[4] Of concern are the sensitivity to various parameters in the inversion setup, limitations in the data, including sparse coverage or artefacts and errors in the transport model. We use a series of test runs with changes in specific setup details, as listed in Table 2.

3.2.1. Sensitivity to the inversion setup. The inversions are sensitive to a range of parameters, most notably the tightness of the a-priori constraint relative to the data constraint, and the scales of the spatial and temporal smoothing imposed by the g functions in eq. (11). As these parameters are chosen somewhat arbitrarily due to the lack of solid independent information, it needs to be shown that our findings persist over a range of reasonable values.

If the a-priori standard deviation is reduced (setup 'tight priors') the amplitude of interannual variations in all three bands is dampened as expected (Fig. 6, panel A). At the same time, the tropical APO flux gets more strongly correlated with ENSO (panel B, 99% significant). Conversely, an increased a-priori standard deviation ('loose priors', not shown) enhances temporal variations but deteriorates the ENSO correlation. This may indicate that the ENSO-related signal component is rather strong, being able to combat the dampening effect of the

[3] Significance has been tested using the algorithm by Ebisuzaki (1997) based on 1 000 000 random realizations of the time-series with the same power spectrum but randomized phase. This takes any serial correlations into account.

[4] These robustness tests focus specifically on the particular features highlighted in Section 3.1. Several other features of the estimated APO fluxes, such as their long-term spatial pattern, are affected by some error sources more strongly. Fortunately, these uncertainties do not represent a problem here because of small a-posteriori correlations with our target quantities; any such cross-influences would be visible in the specific tests shown here.

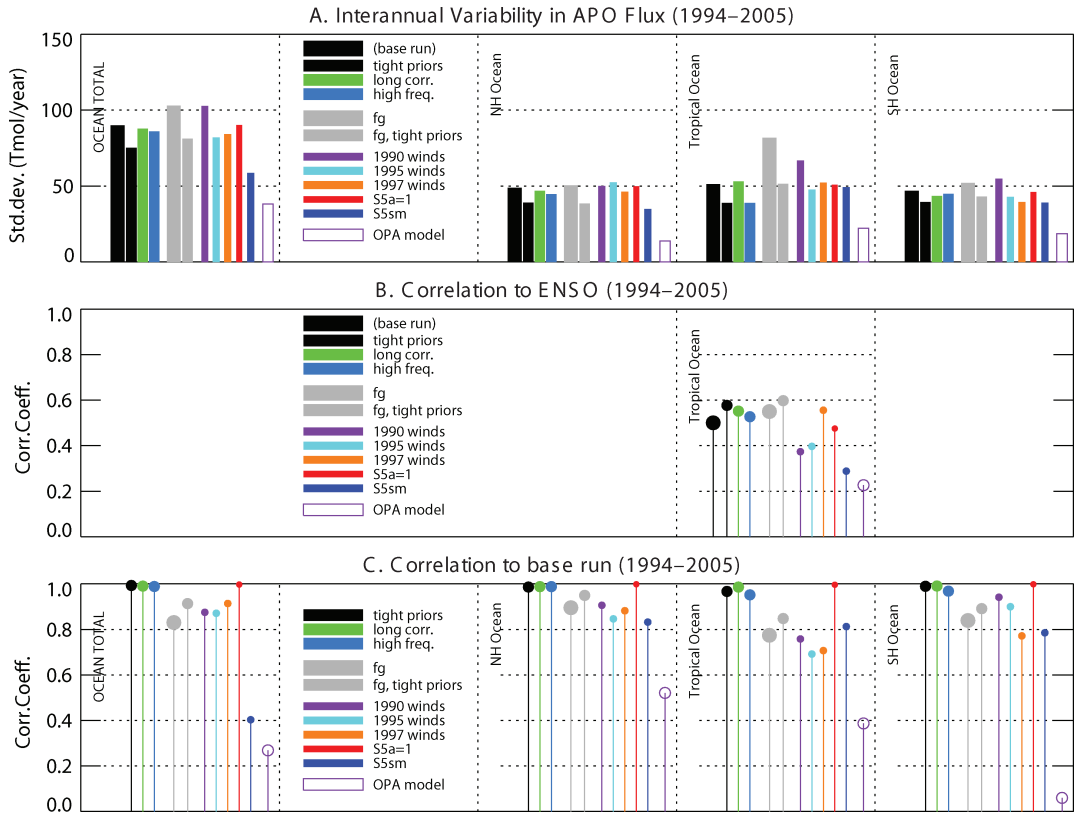

Fig. 6. Statistical properties of retrieved APO fluxes based on five atmospheric sites (S5) for standard and various test cases (Table 2). For the test cases, all parameters are identical to the base run except for the change(s) indicated in the colour code. The hollow symbols give OPA-PISCES-T model results for comparison. The four groups of symbols in each panel correspond to the integration regions as in Fig. 5. (A) Temporal standard deviation (1994–2005) of interannually filtered flux time-series. (B) Correlation coefficients between interannual flux variations (1994–2005) and MEI ENSO index. (C) Correlation coefficients between interannually filtered flux time-series (1994–2005) and that of standard run.

a-priori constraints, whereas loosening of these constraints allows second-order signals, or even errors, to grow.[5] Increasing the a-priori spatial correlation length ('long corr.') does not change the amplitudes much but tends to improve the ENSO correlation. This behaviour is consistent with the large-scale nature of the ENSO phenomenon. Allowing more high-frequency degrees of freedom ('high freq.') reduces amplitudes, but preserves the ENSO correlation. The reduction of amplitudes may arise as model-data mismatches can be satisfied through shorter-term flux variations partly averaging out at the interannual scale.

The ratio of IAV amplitudes in the three latitude bands stays roughly equal for all cases. It should be noted that this ratio may be influenced by the ratio of the chosen a-priori sigma intervals, which is the same among all these cases. To test this influence, further sensitivity cases have been run, setting the 'shape' $\mathbf{f}_{\mathrm{sh,var}}$ for each pixel proportional to the amplitude (temporal standard deviation) of the interannual variations of either the heat flux

[5] The dampening effect of the a-priori constraints on any non-seasonal variability of the oceanic APO flux (i.e. on the signal of interest of this paper) arises because the fixed term $\mathbf{f}_{\mathrm{fix}}^{\mathrm{APO}}$ is deliberately chosen constant on these scales, so that the signal of interest is entirely represented in the adjustable term $\mathbf{f}_{\mathrm{adj}}^{\mathrm{APO}}$. Thus, larger variations (arising from larger parameter values $\mathbf{p}$) lead to a larger cost function contribution in eq. (4) and will be more strongly penalized (cmp. Section 3.3.4. of Rödenbeck, 2005).
The choice of an essentially constant $\mathbf{f}_{\mathrm{fix}}^{\mathrm{APO}}$ reflects the absence of (data-based) a-priori knowledge about IAV of large-scale APO fluxes. It ensures that the retrieved signal of interest represents atmospheric information, rather than a mixture with a-priori signals that would be more difficult to interpret. Is, however, the dampening effect a problem? Indeed, the strength of dampening codetermines the amplitude of the interannual APO flux variations, so that this amplitude is only inferred up to a poorly determined factor. Importantly, however, the features focused on here (ENSO correlation and relative amplitudes) are shown above to be robust against variations in prior strength. The dampening is therefore no problem to the conclusions of this paper.
In a more general view, the additional term in the cost function eq. (4) mathematically corresponds to a Tikhonov regularization (e.g. Hansen, 1998), a device to suppress errors. It works well if signal and noise have distinct properties (e.g. if they vary on different frequency ranges). Unfortunately, such a spectral gap cannot be assumed here, so that dampening the noise involves the risk of dampening the signal. However, if a particular feature (as the ENSO correlation here) persists under increased dampening, it can at least be identified against weaker noise components.

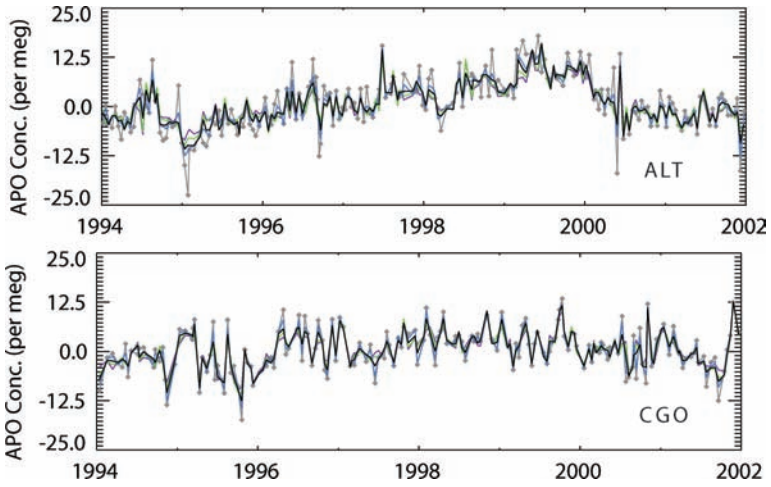

Fig. 7. Examples (stations Alert [top], and Cape Grim [bottom] within eight selected years) illustrating the ability of the inversion to fit the data (Section 2.6). The observations (grey diamonds) are compared to modelled concentrations from the base run (black) and some sensitivity runs (colours similar to Fig. 6: violet–'tight priors', green—'long corr.', light blue—'high freq.'). The mean seasonal cycle and the long-term trend have been subtracted from each line, to highlight the short-term and interannual variations.

from the NCEP reanalysis or of the sea–air APO exchange of the OPA-PISCES-T model (see Section 4.3), respectively (the a-priori flux $\mathbf{f}_{\text{fix}}$ remains without interannual variations as in the standard setup, only the spatial pattern of a-priori sigma intervals is different). The resulting interannual APO flux variations, in particular the amplitude ratio, stay similar to the base run in both cases (not shown). However, this is only a very limited confirmation, because the ratio of the a-priori sigma intervals in the three latitude bands resulting from these two choices is (despite of the differences in the fine structure) roughly similar to that of the base run. Nevertheless, this does confirm that the a-priori assumption of a flat 'shape' in the standard setup is reasonable.

According to panel C of Fig. 6, correlation of IAV of all cases to the base run is mostly high, indicating that the timing and relative amplitudes of anomalies is inferred relatively robustly.

Can we rank the different setups according to their ability to fit the data? Concentrations modelled from all the sensitivity runs (Section 2.6) fit the seasonal cycle and the long-term trend of the APO data well (not shown). The runs differ to some extent in how closely they match the individual data points (Fig. 7), with larger mismatches for the more rigid setups ('tight priors', 'long corr.'), as expected. These differences, however, are mainly in how closely they follow the short-term variations around the slower year-to-year pattern, while that slower variability is similarly captured by all runs. Unfortunately, the rating of the goodness of the fit remains largely subjective: as with inverse methods in general, a close match to the data is desired, while avoiding the 'over-fitting' of noise (e.g. Hansen, 1998). In the present case, there is no external information to distinguish signal and noise, as both may occur at the same timescales. However, the short-term variations are more likely to reflect signals due to local flux features, atmospheric transport or analytical errors. To the extent that this is the case, the less close fit of the 'tight priors' or 'long corr.' setups may indicate an advantage rather than a limitation, in that they manage to extract the larger-scale features.[6] This view is also supported by the finding that runs based on different station sets or different transport model resolutions (to be discussed below), are more closely correlated to each other when using the 'tight priors' rather than the standard setup.

3.2.2. Sensitivity to data errors. Errors in the fluxes can also arise from errors in the observations. It is convenient here to distinguish two classes of errors: those that are correlated between stations and those that are not. The uncorrelated contributions include all sources of random error (e.g. random artefacts during sampling, storage or imprecision of the analysis), as well as many kinds of systematic error (e.g. leaks in the sampling system at a particular site); in addition, a strong influence of local signals in the data could—even if correctly measured—spuriously be interpreted by the inversion as a larger-scale feature. The correlated contribution is likely dominated by errors in laboratory calibration, for example, due to drift in the laboratory reference gases. Calibration drift will impart spurious variability that is nearly synchronous between all stations because flasks are analysed from most stations in the Scripps network with similar time delays after sampling.

To assess the effect of uncorrelated errors, we have carried out inversions with two mutually exclusive sets of sites (SE4 and SE5, see Fig. 1). Due to the lengths of the shortest data records involved, inversions with these limited data sets can only be done over the limited period 1998–2005. The results, shown in Figure 8, column A, yield interannual variability which is generally similar, even in detail, to each other and to the base run. The largest discrepancies are found in the tropics, especially

[6] According to the formalism of Bayesian inference, the model-data mismatch covariance matrix $\mathbf{Q}_c$ should have been chosen to reflect the expected magnitude and timescale of the noise. If this was the case, the goodness of fit could just be assessed by comparison with the sigma intervals. However, for the very difficulties mentioned above, $\mathbf{Q}_c$ just represents a largely arbitrary choice itself.

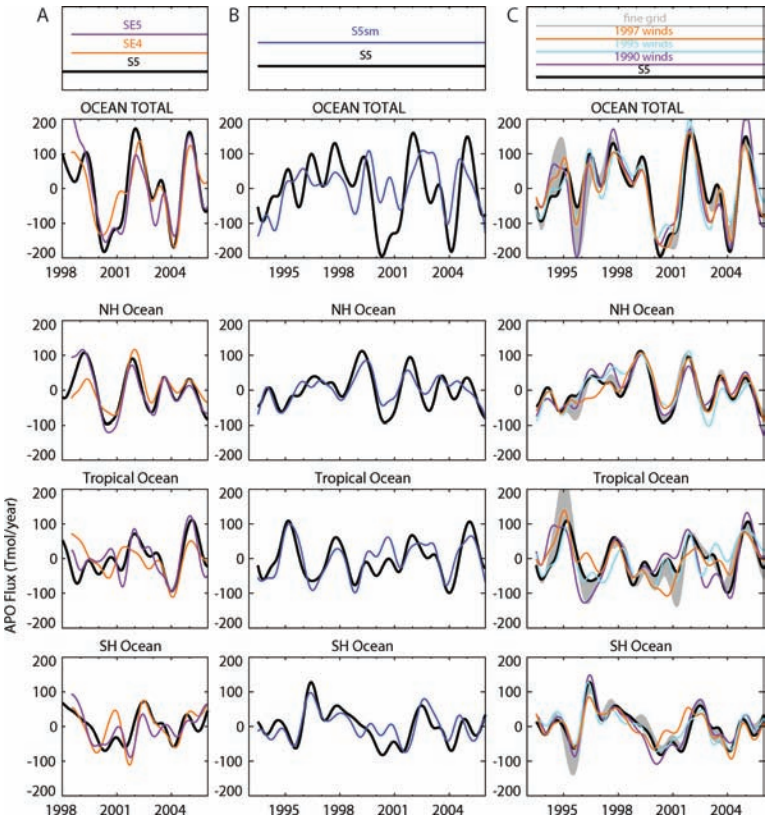

Fig. 8. Testing the robustness of the fluxes shown in Fig. 5 by comparing the base run to sensitivity cases. (A) Results based on two mutually exclusive sets of sites (standard setup). (B) Standard result in comparison with a test run where a global mean APO concentration time-series has been subtracted from all data. (C) Comparison to test runs where atmospheric transport has been simulated with 1990, 1995 or 1997 meteorology used repeatedly. The grey band gives the difference to a sensitivity run using the transport model on finer spatial resolution ($\approx 4^\circ$ latitude $\times 5^\circ$ longitude $\times$ 19 vertical levels).

for the SE4 subset. However, the SE4 network lacks a station near the Equator, and synthetic-data inversions with this network (not shown) also show poor agreement in the tropics. Thus, the larger deviations for SE4 in the tropics are probably just an indication of the poor coverage with this limited network (a test run using the S7 set except for Samoa yields similar behaviour during 1998–2001 as does SE4). The tropical fluxes for SE4 and SE5 both show poorer correlation with ENSO (only discussed qualitatively as the limited available time period 1998–2005 is not sufficient to calculate meaningful correlation coefficients). Interestingly, the correlation with ENSO, even with these limited networks, improves again if the 'tight priors' inversion is used. In any case, these results confirm that the extratropical fluxes are not dominated by site-specific (i.e. uncorrelated) errors or by local signals because these fluxes can be reconstructed quite faithfully with independent networks that share no stations in common. Only the tropical fluxes are potentially impacted by site-specific errors. In the tropics, however, the strong correlation with ENSO helps to establish the reliability of the fluxes. The conclusions from the comparison of the mutually exclusive sets are corroborated by the fact that the larger sets S7 and S9 mainly confirm the results of set S5.

An examination of the stability of the reference gases used at Scripps suggests that, although the gases appear stable over the long term, shorter-term drift at the level of ± 2 per meg is possible (Keeling et al., 2007). This is comparable to the observed variability in the global average APO. Thus, the inferred variability in total ocean APO flux is near the threshold of detectability.

To assess the impact of correlated errors, we have carried out a run (S5sm) in which the global mean APO concentration has been subtracted from all stations (set S5). The global mean is based on the average of all five stations, with the data points weighted as in the inversion and the resulting global time-series smoothed with a 3 month running average (triangular pulse response function). Run S5sm effectively makes the extreme assumption that the variability in the global average APO is entirely due to laboratory calibration artefacts. As shown in Fig. 6 (panels A and C), run S5sm yields fluxes within the three major zones that are quite similar to the base case. The within-zone variability is evidently tied to station-to-station differences, which are not sensitive to the stability of the laboratory calibration.

The total ocean flux, however, is found to be considerably smaller using S5sm. Thus, although the fluxes within the individual zones are not sensitive to the stability of the laboratory calibration, their sum, as reflected in the ocean total, is quite sensitive. Nevertheless, there is indirect evidence that the inferred variability of the total ocean APO flux is realistic. First, the tropical fluxes found with S5 show a considerably stronger correlation to the ENSO index than those found with S5sm. Second, the quadrature sum of the variability within the individual zones matches the global variability almost perfectly in the S5 case, but the quadrature sum is larger by 30% in the S5sm case. To account

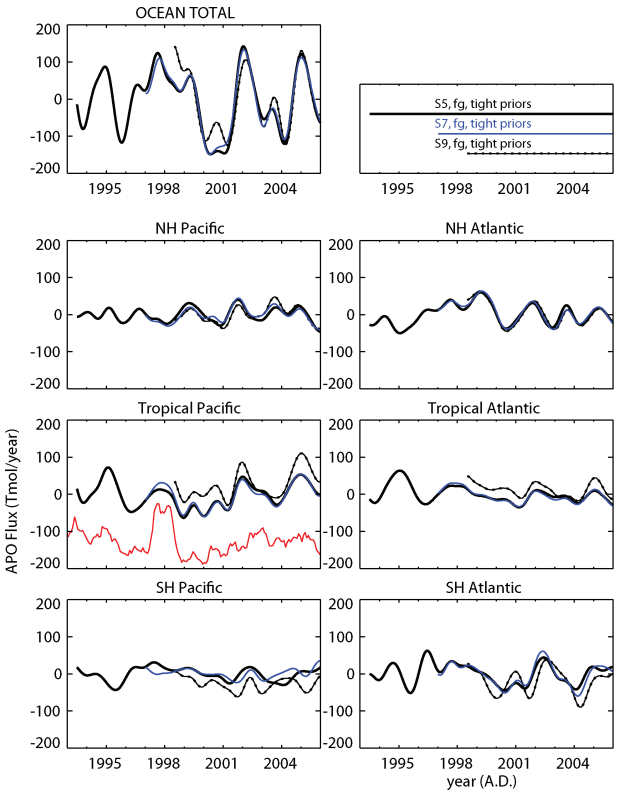

Fig. 9. Interannual APO flux variation as Fig. 5, but each latitude band split into a Pacific (left-hand panel) and Atlantic plus Indian (right-hand panel) contribution. Moreover, the standard setup has been replaced by 'tight priors' and the transport model has been run at finer spatial resolution.

for these results assuming that the total ocean APO variability is artefactual (as for S5sm), the strong correlation with ENSO and the matched quadrature sum must both be dismissed as coincidence. This requires that, by chance, the calibration gases drifted with a temporal pattern that produced a spurious correlation to ENSO in exactly the latitude band where a correlation makes the most sense mechanistically, and they drifted with an amplitude that achieved a match in the global quadrature sum. Furthermore, one must accept that there are teleconnections between the zones that cause fluxes in the different zones to be anti-correlated, thus yielding global variability that is smaller than expected from the sum of the zonal variations. In contrast, if the observed global APO variability is accepted at face value (as for S5), a satisfying result is obtained that the global variability can be attributed to independent contributions from the different zones, and the tropical variability is found to correlate with ENSO. No teleconnections or coincidences are implied. On this basis it seems likely that the variability in global APO flux indicated by the base run is realistic.

3.2.3. Sensitivity to transport model errors. Estimated APO flux variability may be affected by transport model errors. In particular, as atmospheric transport also varies with ENSO, the concern arises whether the ENSO correlation in our flux estimates actually arises from model errors rather than from the atmospheric data. To explore this possibility, additional inversions were run using meteorological driver data from fixed years (1990, 1995 and 1997 as arbitrary selections), applied repeatedly to all years of the simulation (thinner bars in Fig. 6; see time-series in Fig. 8 column C). Though this is expected to degrade the result, the flux fields are not fundamentally changed, with similar variability and with a considerable correlation to the base run (0.7 in the tropics and higher elsewhere). The correlation to ENSO is reduced in two cases (1990 and 1995, remaining at least 90% significant) and slightly enhanced in one (1997). Such a situation would be very unlikely if the ENSO correlation would result from modelled transport variability.[7]

How large is the overall magnitude of errors induced by the transport model? For latitudinal and seasonal APO variations, for example, Battle et al. (2006) or Nägler et al. (2007) concluded from comparing forward simulations with different transport models that model errors are larger than the differences corresponding to using different flux data sets (such as Garcia and Keeling, 2001 or different ocean process models). The resulting difficulty of estimating spatial patterns of long-term fluxes has long been recognized as a general limitation of inversions (e.g. Bousquet et al., 2000). To obtain a lower limit of the influence of transport model errors on the particular flux features considered here, we conducted a run at finer spatial resolution of the model ('fg', $\approx 4^\circ \times 5^\circ$). Any difference to the base run can only be due to model errors. Again most features in the interannual variability are preserved, with the largest changes being in the tropics (Fig. 6). The correlation of the tropical fluxes to ENSO is slightly enhanced while the magnitude of the tropical fluxes is increased.[8] Effects of transport model errors on the amplitude of interannual and seasonal variability are also discussed in Section 4.3.

Further, as a sizable fraction of conceivable model errors are site-specific (representation of the local circulation determining transport pathways and signal dilution, errors due to matching the nearest model grid box value and a point measurement), we can again invoke the test with the exclusive sets SE4 and SE5 in

[7] These tests cannot rule out, however, the possibility that the ENSO-related signal in the data is dominated by atmospheric transport in reality, but that this transport influence is grossly underestimated by the model both with and without interannually varying meteorology.

[8] The increase in tropical amplitude is largely due to the much higher peak around 1995 (Fig. 8 column C). This peak is over-proportionally dampened as soon as the 'tight priors' setup is used (cf. Fig. 9), suggesting that it is a less robust feature. As a consequence, the model resolution influence is smaller with 'tight priors' (higher correlations to base run, Fig. 6 panel C, and more similar amplitudes, panel A). Incidentally, the higher-resolution 'tight priors' case shows the highest ENSO correlation of all runs considered.

Section 3.2.2 showing that such errors do not dominate the flux features considered here.

3.2.4. Sensitivity to O_2 : CO_2 *stoichiometry.* Any deviation of the actual O_2 : CO_2 stoichiometry from the assumed factor of 1.1 in the APO definition will lead to incomplete cancellation of land signals, which will then spuriously be projected by the inversion into ocean fluxes. As a particular concern, the estimated tropical APO variability could be caused this way, as tropical land CO_2 fluxes show large interannual variations closely correlated to ENSO. The magnitude of the possible effect has been assessed by a run where APO data have been calculated with a factor 1.0 (in the fixed terms of the flux model, the factor has not been changed). Figure 6 reveals that this hardly changes the result (almost full correlation to the base run), and the conclusions about IAV amplitudes and ENSO correlations get confirmed (the main change is a shift in the long-term flux of the Northern Hemisphere, where the land fraction is highest). This conclusion would still hold for values of 0.9 or 1.3 which would lead to twice the absolute change. Though the O_2 : CO_2 stoichiometry may differ among physiological processes (photosynthesis, autotrophic or heterotrophic respiration, biomass burning) or vary seasonally or interannually, this will likely lead to errors of the same order of magnitude only.

4. Discussion

4.1. Contributions to APO flux variability

A variety of processes can contribute to the air–sea exchanges of O_2, CO_2 and N_2 that drive APO variability. Photosynthesis in surface waters drives O_2 outgassing and CO_2 ingassing, whereas the ventilation of subsurface waters impacted by respiration drives O_2 ingassing and CO_2 outgassing. Warming will tend to drive outgassing of all three gases, due to solubility effects, whereas cooling drives ingassing. Air–sea CO_2 exchange is also driven by the changes in atmospheric CO_2 concentration and is heavily influenced by chemistry of the carbonate system in seawater. A small contribution to the exchange of these gases may arise from changes in salinity, barometric pressure or from bubble processes.

On seasonal timescales, APO variability is clearly dominated by O_2 exchanges due to three factors: (1) the larger temperature dependence of the solubility of O_2 compared with N_2, (2) the tendency of dissolved O_2 to equilibrate more rapidly with the atmosphere than dissolved CO_2 buffered by the carbonate chemistry, and (3) the tendency for the thermal, dynamic and biological effects to reinforce each other in driving O_2 exchange (e.g. spring warming is accompanied by reduced mixing and enhanced photosynthesis, all leading to O_2 outgassing) but to counteract each other in driving CO_2 exchange (e.g. spring warming counteracts the reduced mixing and enhanced photosynthesis for CO_2 fluxes; Keeling et al., 1993). The situation is schematically depicted in Fig. 10.

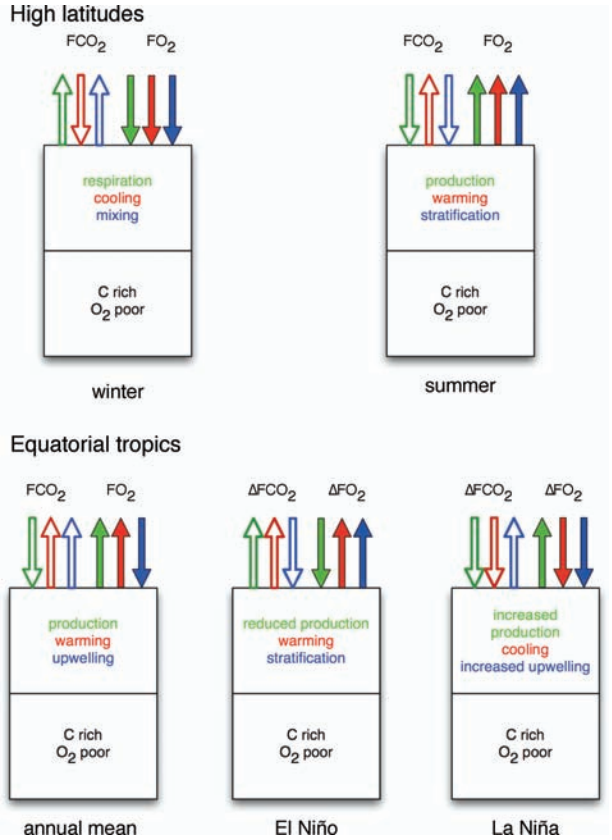

Fig. 10. Illustration of the response of the sea–air CO_2 exchanges (hollow arrows) and O_2 exchanges (solid arrows) to the seasonality in the high latitudes (top panels, giving winter and summer situations) and to the ENSO cycle in the tropics (bottom panels, giving annual means and respective deviations). The different colours indicate the respective contributions due to changes in biology (green), thermodynamics (red) or dynamics (blue). The full line in the middle of each panel separates the surface mixed layer from the deep ocean. In the case of O_2 exchanges in the high latitudes, all three processes act together, whereas O_2 exchanges in the tropics result from competing effects (upwelling effect in a narrow band along the equator, production and warming effects in the adjacent bands to the North and South). In contrast, CO_2 exchanges involve competing effects everywhere.

On the interannual timescale emphasized by our inversions, O_2 exchanges are also expected to be more important than those of CO_2 and N_2. All three factors listed above are also relevant on interannual timescales. Keeling and Severinghaus (2000) have shown that ocean biological processes will tend to drive larger O_2 than CO_2 fluxes on all timescales from seasonal to millennial, due to the slow equilibration rate and large oceanic absorption capacity for CO_2 as opposed to O_2. Although the increase in atmospheric CO_2 drives a large global air–sea CO_2 flux that dominates the global air–sea exchange of APO on decadal timescales (e.g. Manning and Keeling, 2006), the variations in atmospheric CO_2 are too small to be very

important in driving APO fluxes on the shorter timescale emphasized here.

The importance of O_2 flux in driving the APO variability is also supported by a comparison of the inversion results with inferred variability in air–sea CO_2 exchange. In the tropical Pacific, CO_2 flux variability, expressed as a standard deviation, is estimated to be of the order of ± 10 to ± 20 TmolC yr^{-1} and is dominated by El Niño phenomenon (Feely et al., 2006). Air–sea exchange of CO_2 in the tropical Pacific is therefore sufficient to account for only a fraction of the tropical APO variability of ± 50 Tmol yr^{-1} inferred from this inversion. In the extratropics, CO_2 flux variability is less well constrained from observations but the contributions of the northern and southern extratropics to the global variability are probably not individually greater than the contribution from the tropical Pacific. If so, CO_2 can also make only a small contribution to APO flux variability in the extratropics.

In fact, it seems reasonable that CO_2 could make a larger contribution to interannual APO variability in the tropics than in other latitude bands. The Equatorial Pacific is an exception to the general tendency for thermal, dynamic and biological forcing to have reinforcing effects on O_2 flux and cancelling effects on CO_2 flux (Feely et al., 2002). Here, the upwelling along the Equator of O_2-undersaturated waters drives a net O_2 ingassing which is counteracted, not reinforced, by simultaneous warming of the waters and biological production (Stephens et al., 1998, see also Fig. 10). The warming, however, reinforces the outgassing of CO_2 from the upwelled, CO_2-supersaturated waters, though it is compensated by biological processes. Outside the tropics, the APO flux variability is probably mostly driven by variations in seasonal production and ventilation processes, because these processes would reinforce each other for O_2 but cancel each other for CO_2 (Takahashi et al., 2002). The APO flux variability driven by variations in Equatorial upwelling (e.g. by ENSO) could therefore be unique in containing a relatively large CO_2 contribution.

The interannual APO flux variability was found to be similar in the three ocean bands. However, this does not necessarily imply that the CO_2 flux variability is similar. In fact, if CO_2 makes a larger contribution to the APO variability in the tropics, our results would then support the conclusion that tropics dominate the sea–air CO_2 flux variability.

The similarity in amplitude of the APO variability in the northern extratropics to that of the other latitude bands is remarkable as its ocean area is smaller (24%, 37% and 39% for the northern, tropical and southern bands, respectively). Comparing the two extratropical bands to each other, the similar amplitudes of interannual variability are consistent with the similar amplitudes of seasonality (Fig. 13, Appendix D). Hamme and Keeling (2008) identify interannual variations in ventilation likely to be the most important driver of the interannual APO fluxes. However, a high per-area variability in biological processes would also be supported, by the high biomass of the Northern hemisphere induced by a relatively well stratified ocean in the Northern summer, especially in the North Atlantic[9] (e.g. Behrenfeld et al., 2006).

4.2. *Relation of the APO flux to climate variability*

The correlation that we find between tropical APO flux and the El Niño index appears statistically robust, although the correlation coefficient is not high, as expected for a complex mechanism resulting in non-linear relationships: The effect on O_2 exchange is not necessarily proportional to the strength of an El Niño event. For the strong 1997/1998 El Niño, in particular, there is no correspondingly strong APO flux anomaly; when omitting a 1- or 2-yr time interval around this event from the computation of the correlation coefficients, they tend to slightly increase (in particular for the 'fg' results). As a corollary, the Spearman rank correlation (with less emphasis on amplitudes) yields higher correlation coefficients than the linear correlation shown here. Interestingly, an El Niño signal is not manifest in the APO anomalies at any individual site, so is retrieved by the inversion from the differences in APO between stations (cf. Hamme and Keeling, 2008).

The sign of the El Niño response comes as somewhat of a surprise. Keeling et al. (1993) predicted that equatorial upwelling should result in a net release of O_2 to the atmosphere, driven by the supply of preformed nutrients in the upwelling waters. This prediction was supported by the studies of Battle et al. (2006) and Tohjima et al. (2005), which verified the existence of an atmospheric APO maximum in the tropical Pacific, evidently tied to the equatorial upwelling. If tropical upwelling causes O_2 outgassing, how can the weakening of upwelling during El Niño events cause even more O_2 outgassing? These earlier studies recognized that the O_2 outgassing resulted from fluxes of different sign in different regions. In the intense upwelling region along the Equator in the eastern tropical Pacific, upwelling causes surface waters to be undersaturated in O_2, leading to net O_2 uptake by the oceans. This ingassing is evidently more than compensated on average by outgassing of O_2 driven by continued warming and biological production in the upwelled waters as they spread outward from the intense upwelling regions (Stephens et al., 1998; Najjar and Keeling, 2000). An increase in

[9] Indeed, more than half of the northern extratropical variability is attributed to the Atlantic (Fig. 8), despite of the greater area of the North Pacific. This is a tentative finding, as the inferred flux variations for Atlantic and Pacific actually share many features and as our station set lacks longitudinal extent (though changing wind directions at ALT and CBA conceivably impart some differential information). At least, the inferred Pacific–Atlantic split is found to be robust with respect to the sensitivity tests considered above (not shown), and some ability to separate the northern extratropical Pacific and Atlantic is supported by the synthetic inversions (Appendix C). Improvements in the longitudinal resolution are expected from the addition of further atmospheric sites. In any case, corroboration of the flux variability from the inversion by independent approaches would be desirable.

O_2 outgassing during El Niño events can therefore be explained if the O_2 exchange with the atmosphere is more strongly modulated in the intense upwelling regions than in the surrounding waters. This is possible if the time lag between upwelling and eventual O_2 outgassing is longer than a typical El Niño event.

The APO fluxes can be compared with recent estimates of interannual changes in ocean biological productivity. During the strong El Niño to La Niña transition of 1998–1999, when we infer from the APO inversions that the tropical oceans were an anomalously large sink for atmospheric O_2, the satellite observations indicate that a simultaneous increase of order 200 TmolC yr^{-1} occurred in net primary production (NPP) over a broad band in the Pacific from 30°N to 30°S (Behrenfeld et al., 2006). An increase in production would tend to drive an outward rather than inward flux of O_2. Only the fraction of NPP that is exported from the upper ocean can influence APO, because the recycled production has no effect on O_2 and CO_2 concentrations. In tropical waters, this fraction is typically ≈10% (Laws et al., 2000), which suggests that the increase in export production associated with the 1998–1999 transition was of order 20 TmolC yr^{-1}. This estimate is small compared to the change in APO flux over this period, which from Fig. 5 is ≈100 Tmol/yr. The comparison both in amplitude and in direction suggests that changes in production are not the primary control on the APO flux. Rather the fluxes must be principally driven by changes in the delivery of O_2-undersaturated water to the surface, as discussed above, though partially offset by changes in photosynthesis.

4.3. Comparison to the OPA-PISCES-T ocean process model

To illustrate the potential for APO fluxes to test ocean models, we briefly compare the inversion results to the predictions of the OPA-PISCES-T model. The OPA-PISCES-T model is a global ocean general circulation model (OPA) coupled to an ocean biogeochemistry model (PISCES-T). The simulations presented here are identical to those published in Le Quéré et al. (2007). OPA has a resolution of 0.5°–1.5° latitude × 2° longitude and 30 vertical levels. It computes mixing along isopycnal surfaces, includes a parametrization for eddy mixing (Gent and McWilliams, 1990) and computes explicitly vertical turbulence and the mixing depth with a 1.5 order turbulent kinetic energy model (Gaspar et al., 1990). OPA is coupled to a dynamic-thermodynamic sea-ice model (Fichefet and Maqueda, 1999). PISCES-T represents the full cycles of C, O_2, P, Si, total alkalinity and a simplified Fe cycle. It also includes a representation of two phytoplankton (silicifiers and mixed), two zooplankton (micro and meso) and three types of dead organic particles of different sinking rates. OPA-PISCES-T is forced by daily winds and precipitation from NCEP reanalysis (Kalnay et al., 1996). Heat fluxes and evaporation are computed with a bulk formula that is a function of the difference between sea surface temperature produced by the model and the 2 m air temperature from NCEP. These model simulations reproduce the observed interannual variability in CO_2 in the equatorial Pacific (Feely et al., 2006) and the lower amplitude of variability inferred from observations in the North Pacific and Southern Ocean (McKinley et al., 2006; Le Quéré et al., 2007) but not the variability of the North Atlantic (Schuster and Watson, 2007). For comparison purposes, the daily fluxes predicted by the OPA-PISCES-T model were temporally filtered and spatially integrated over the same three zones as the inversion calculations. The period of this comparison is 1993–2005, identical to our base inversion run.

The OPA-PISCES-T model yields variations in APO flux that, consistent with the theoretical considerations, are dominated by fluxes of O_2. The variations in air–sea O_2 flux are roughly 4.4, 1.4 and 4.4 times greater than the CO_2 flux in the north, tropical and southern bands, respectively. In the extratropics, the CO_2 and O_2 fluxes are strongly anti-correlated, as expected due to variations in marine photosynthesis or ventilation. Here the variations in APO flux are closely tied to the variation in O_2 flux but slightly smaller in magnitude. In the tropics, the modelled CO_2 and O_2 fluxes are only weakly anti-correlated. Here the variations in APO fluxes are slightly larger than O_2 flux variability, but the two are evidently not so closely tied to one another.

However, the model-predicted variations in APO flux are considerably smaller than those inferred from the inversions (hollow bars in Fig. 6 panel A). The variability in APO flux inferred from the base inversion, expressed as a standard deviation, exceeds that from the OPA-PISCES-T model by factors of 3.5, 2.3 and 1.8 in the northern, tropical and southern bands, respectively. In contrast to the inversion, the variability in modelled APO fluxes in the northern and southern extratropics is more nearly equal in a per-area sense. The discrepancies seem larger than the uncertainties in the inversions, as implied by the sensitivity analysis. In contrast to results from the base inversion, tropical APO fluxes as modelled by OPA-PISCES-T are much more weakly correlated with the MEI index (Fig. 6, panel B). In fact, the OPA-PISCES-T model fluxes are only moderately correlated to the inversion results in any band.

The OPA-PISCES-T model comparison raises the question whether the inversion results overestimate the flux variability because of deficiencies that were not addressed in the sensitivity studies. For example, could the TM3 transport model systematically overestimate vertical or land–ocean mixing, which would require spuriously large surface fluxes to account for the surface APO observations at marine sites? TM3 simulates reasonably well the change in the amplitude of the CO_2 seasonal cycle with elevation, which is diagnostic of vertical mixing over the continents (Stephens et al., 2007). A diagnostic of vertical mixing over the oceans and land–ocean mixing is provided by the seasonally varying air–sea fluxes of O_2 in the extratropics, as estimated by the inversion. We find that the seasonal

amplitudes in the two extratropical bands are robust within around 20% to aspects of the inversion setup and to the station set, so hinge principally on the transport model. Compared with the ΔpO_2-based O_2 flux climatology of Garcia and Keeling (2001), the seasonal amplitudes of the inversion are larger by a factor of around 1.6 in the Northern Extratropics and similar in the Southern Extratropics (note that this flux climatology has been used in the spatial weighting of the seasonal amplitudes and is therefore not independent, but the robustness of the estimated seasonal amplitudes to prior tightness shows that they are not determined by this a-priori setting). The fluxes of Garcia and Keeling (2001) are not without uncertainty (e.g. they critically depend on the chosen gas transfer parametrization), but the comparison raises the possibility that the transport model has too much mixing in the northern hemisphere. However, the impact of this deficiency on the interannual variability is certainly smaller than that on the seasonality, because the interannual signals have more time to mix uniformly throughout the hemisphere. On this basis, it seems unlikely that the interannual variability is in error by more than a factor of 1.5 due to transport deficiencies. Measurements of APO over continents and aloft would provide useful diagnostic information.

Our analysis suggests that OPA-PISCES-T underestimates the variability in APO fluxes by a factor of 1.8 to 3.5, with largest underestimation at high Northern latitudes. The variability of CO_2 and O_2 fluxes in OPA-PISCES-T is at the upper end of variability estimated by other global ocean biogeochemistry models (McKinley et al., 2000, 2006; Peylin et al., 2005), thus suggesting that existing models share the same deficiencies as OPA-PISCES-T.

Possible reasons for the deficiencies in APO variability include: (1) known problems in representing variability in biological processes, probably caused by the tight feedbacks between biological export production and ocean physics in current models (Le Quéré et al., 2005) and the simplistic representation of ecosystem response to climate variability, (2) poor horizontal resolution in the physical model, which does not allow for an explicit representation of eddies and their associated turbulent fluxes and (3) possible lack of very high resolution in atmospheric forcing. These problems would have a larger effect on interannual variations in O_2 compared with CO_2 because of the faster equilibration rate of O_2 and because of the reinforcement of thermal, dynamic and biological processes in O_2 fluxes at high latitudes (over time-scales of centuries or longer, both gases would be equally affected).

The variability in APO fluxes provides stronger constraints on process models than variability in CO_2 fluxes because the processes driving APO variability reinforce one another and amplify potential deficiencies in physical models. Observations of APO variability provide new constraints which hopefully will help to improve global biogeochemistry models and their response to climate variability on seasonal to millennial time-scales.

5. Conclusions

We estimated the regional contribution of the ocean to the interannual variability in APO using up to nine atmospheric measurement sites and an inverse method. Most of this variability is caused by changes in sea–air O_2 fluxes.

(1) The data used here are sufficient to constrain interannual flux variations in three latitudinal bands (90° S–20° S, 20° S–20° N, 20° N–90° N), tentatively with some ability to also resolve Pacific and Atlantic in the northern band.

(2) A significant and robust correlation has been found between tropical APO fluxes and ENSO (MEI index), suggesting that most of the tropical variability is caused by the ventilation of subsurface O_2 from El Niño-induced changes in equatorial upwelling.

(3) Interannual variations in the northern and southern extratropical bands are estimated to be of similar amplitude than in the tropical band, where a larger part of the variability in APO in the Northern hemisphere would be caused by variability in marine biology.

(4) Our results further suggest that current ocean biogeochemistry models underestimate the interannual variability in O_2 fluxes in all oceanic basins (by about a factor of 2 in the tropics and Southern Hemisphere and at least 3 at high Northern latitudes), with maximum discrepancy in the North Atlantic.

Further steps will profit from including further sites from other atmospheric O_2 measurement programmes (e.g. Bender et al., 1994; Tohjima et al., 2003).

6. Acknowledgments

We thank A. Manning for his contributions to the Scripps oxygen measurement program and for interesting discussions. We thank E. Buitenhuis for performing various OPA-PISCES-T model runs. Interesting and helpful discussions with M. Battle, M. Bender, L. Bopp, N. Cassar, B. Stephens and Y. Tohjima about oxygen measurement and interpretation are gratefully acknowledged. The paper profited from helpful comments by the two anonymous referees.

7. Appendix A: Linking measured and modelled quantities

Throughout this paper, M^{O_2}, M^{CO_2} and M^{N_2} denote the amount (number of moles) of the respective species in an air parcel or air sample, or model grid cell. CO_2 measurements are usually reported as molar mixing ratios on an H_2O-free basis defined as

$$X^{CO_2} = \frac{M^{CO_2}}{M^{air}}, \tag{A1}$$

with

$$M^{air} = M^{N_2} + M^{O_2} + M^{CO_2} + \ldots, \tag{A2}$$

where the dots represent minor constituents of air other than H_2O, and which can be neglected in practice. Molar mixing ratios are always given in ppm = μmol mol^{-1} here. For the abundant gases O_2 and N_2, the molar mixing ratio is not an appropriate measure, because it is also changed by any changes in the other gases included in the denominator, where the ratio of changes is given by the molar mixing ratio of the (abundant) gas itself. Therefore, O_2 measurements are reported as changes in O_2/N_2 ratio according to (Keeling and Shertz, 1992)

$$\delta(O_2/N_2) = \frac{(O_2/N_2) - (O_2/N_2)_{\rm ref}}{(O_2/N_2)_{\rm ref}} 10^6 \,\text{per meg}, \tag{A3}$$

where

$$(O_2/N_2) = \frac{M^{O_2}}{M^{N_2}} \tag{A4}$$

denotes the ratio of the oxygen and nitrogen amounts in the sample and $(O_2/N_2)_{\rm ref}$ the corresponding ratio in the reference gas. The 'per meg' unit specifically refers to this very definition. In a similar way, APO measurements are reported as (Stephens et al., 1998)

$$\delta(\text{APO}) = \delta(O_2/N_2) + 1.1(X^{CO_2} - X_0^{CO_2})\frac{10^6 \text{per meg}}{X_0^{O_2}}. \tag{A5}$$

The arbitrary reference value

$$X_0^{CO_2} = 350\,\text{ppm}, \tag{A6}$$

for the CO_2 molar mixing ratio has been introduced for convenience but cancels out for the concentration differences relevant here. As a further parameter, this definition contains a fixed reference oxygen mixing ratio set to

$$X_0^{O_2} = 209\,460\,\text{ppm}. \tag{A7}$$

To establish the relation between the APO concentration δ(APO) and trace gas fluxes to be modelled, we observe that changes in δ(APO) are related to (flux-induced) changes ΔM in the abundances of oxygen, carbon dioxide and nitrogen by

$$\begin{aligned}
&\Delta\delta(\text{APO}) \\
&= \frac{\partial\delta(\text{APO})}{\partial M^{O_2}}\Delta M^{O_2} + \frac{\partial\delta(\text{APO})}{\partial M^{CO_2}}\Delta M^{CO_2} + \frac{\partial\delta(\text{APO})}{\partial M^{N_2}}\Delta M^{N_2} \\
&= \frac{\Delta M^{O_2}}{M^{\rm air}}\left[\frac{(O_2/N_2)}{(O_2/N_2)_{\rm ref}}\frac{X_0^{O_2}}{X^{O_2}} - 1.1X^{CO_2}\right]\frac{10^6\,\text{per meg}}{X_0^{O_2}} \\
&+1.1\frac{\Delta M^{CO_2}}{M^{\rm air}}\left[1 - X^{CO_2}\right]\frac{10^6\,\text{per meg}}{X_0^{O_2}} \\
&-\frac{X_0^{O_2}}{X_0^{N_2}}\frac{\Delta M^{N_2}}{M^{\rm air}}\left[\frac{(O_2/N_2)}{(O_2/N_2)_{\rm ref}}\frac{X_0^{N_2}}{X^{N_2}}\right. \\
&\qquad\left.+\frac{X_0^{N_2}}{X_0^{O_2}}1.1X^{CO_2}\right]\frac{10^6\,\text{per meg}}{X_0^{O_2}}.
\end{aligned}$$

where the partial derivatives follow from eqs. (A1), (A3)–(A5) and have been slightly expanded, in the last line introducing a nitrogen reference mixing ratio set to

$$X_0^{N_2} = 790\,190\,\text{ppm}. \tag{A8}$$

The expansion has been done so that the factors in square brackets are close to one: assuming anti-correlated changes in CO_2 and O_2 mixing ratios on the order of $\Delta X \approx 10$ ppm (i.e. $X^{CO_2} \approx X_0^{CO_2} + \Delta X$ and $X^{O_2} \approx X_0^{O_2} - \Delta X$), as well as $(O_2/N_2)_{\rm ref} \approx X_0^{O_2}/X_0^{N_2}$ and $X^{N_2} \approx X_0^{N_2}$, these factors can be approximated by unity with a relative error on the order of 10^{-4}. Further, the expansion singles out the factor

$$\frac{10^6\text{per meg}}{X_0^{O_2}} = \frac{1}{0.209\,460\frac{\text{ppm}}{\text{per meg}}} = 4.7742\,\frac{\text{per meg}}{\text{ppm}}, \tag{A9}$$

which relates to a change of units. For technical convenience, we removed this factor by converting measured APO into

$$c_{\rm obs}^{\rm APO} = 0.209\,460\frac{\text{ppm}}{\text{per meg}}\cdot\delta(\text{APO}), \tag{A10}$$

directly comparable to the usual 'ppm' based model output. According to the above discussion, changes in $c_{\rm obs}^{\rm APO}$ are related to changes in the amounts of O_2, CO_2 and N_2 by

$$\Delta c_{\rm obs}^{\rm APO} = \frac{\Delta M^{O_2}}{M^{\rm air}} + 1.1\cdot\frac{\Delta M^{CO_2}}{M^{\rm air}} - \frac{X_0^{O_2}}{X_0^{N_2}}\cdot\frac{\Delta M^{N_2}}{M^{\rm air}}, \tag{A11}$$

with sufficient accuracy.

The atmospheric transport model simulates changes ΔM in the abundance of any constituent in all its grid cells resulting from given surface fluxes **f**. Due to linearity of transport, the relation (A11) can be reproduced by using the linear combination eq. (5) of fluxes.

Since the modelled air mass $M_{\rm mod}^{\rm air}$ in the grid cell is derived from the cell's horizontal size and vertical pressure gradient, it neglects the actual changes in $M^{\rm air}$ generated by fluxes of O_2, CO_2 and N_2. This introduces another error that, however, is on the same order as the above-mentioned simplifications.

8. Appendix B: Implementation details

B.1. Concentration uncertainty

The main importance of the covariance matrix $\mathbf{Q_c}$ in the cost function eq. (2) is its role as a weighting among the individual data points. It has been specified here in a way analogous to the CO_2 inversion (Rödenbeck, 2005). Concentration mismatch uncertainties with respect to an individual value (i.e. diagonal values of $\mathbf{Q_c}$) are specified as a quadratic sum of assumed measurement and model uncertainties. Assumed measurement uncertainty is always set to 0.4 ppm. Assumed model uncertainty depends on a site class reflecting the expected difficulty for the model to simulate the concentration field at the sites' location, given in Table 1. Standard values are 1.5 ppm for class R ('remote') and 2.25 ppm for S ('shore'). These values are proportional to those of the CO_2 inversion of Rödenbeck (2005), assuming that the ratio of model errors between sites classes is

sufficiently similar for APO and CO_2 (taking into account that the assumptions underlying these numbers are rough anyway, and that a common factor multiplying the whole matrix $\mathbf{Q_c}$ has less importance). Finally, a data density weighting is applied: If there is more than one data value within three weeks, the corresponding diagonal values of $\mathbf{Q_c}$ are artificially increased, to reduce the effect of varying data density in time (mainly relevant for continuous measurements). All off-diagonal elements of $\mathbf{Q_c}$ are set zero, meaning that any error correlations in measurements or model simulations are neglected.

B.2. Initial atmospheric concentration

The initial state of the atmosphere in the transport model (at the beginning of the runs in 1992) is chosen to be uniformly mixed with an APO concentration of −21 ppm. A uniform initial concentration is convenient as it is not changed by subsequent transport, thus just leading to a constant offset at any location and time, so that all elements of the vector $\mathbf{c}_{\mathrm{ini}}$ in eq. (1) have the same value. The mismatch between this initial concentration field and the real one is accounted for by introducing some additional adjustable flux within the first half year of the simulation. The first year of fluxes, which is influenced by spin-up effects, is never used in any analysis of the results.

9. Appendix C: How much detail can be resolved?

The performance of the method to estimate APO fluxes has been tested by replacing the measurements $\mathbf{c}_{\mathrm{obs}}$ by synthetic data, which have been created by a transport model simulation based on a given set of APO fluxes (the 'known truth'). These pseudo-data are taken at the same locations and times as the real data, thus representing the same amount of information. The APO flux chosen as 'known truth' is intended to be similar to the real flux (interannual and high-frequency variations of O_2 from the OPA-PISCES-T ocean process model simulation, see Section 4.3, mean and seasonality of O_2 from Garcia and Keeling, 2001, CO_2, N_2 and fossil-fuel contributions as the fixed terms of the standard flux model, Section 2.4.2). Inverting such pseudo-data is instructive as the correct answer would be a reconstruction of the known truth. Moreover, the transport model can then be assumed to be error-free. Therefore, discrepancies between retrieved fluxes and the 'known truth' reveal which flux features cannot be 'seen' by the available amount (spatial and temporal coverage) of atmospheric information or hint at limitations in the degrees of freedom built into the flux model.

Figure 11 shows 'synthetic' inversion estimates for station sets S5, S7 and S9 (Fig. 1), to be compared with the 'known truth' in white. It can be seen that the seasonality (three selected years in column A) is almost perfectly reconstructed. High-frequency variations present in the 'known truth' are however missing: they cannot be retrieved from the mainly two-weekly data and have

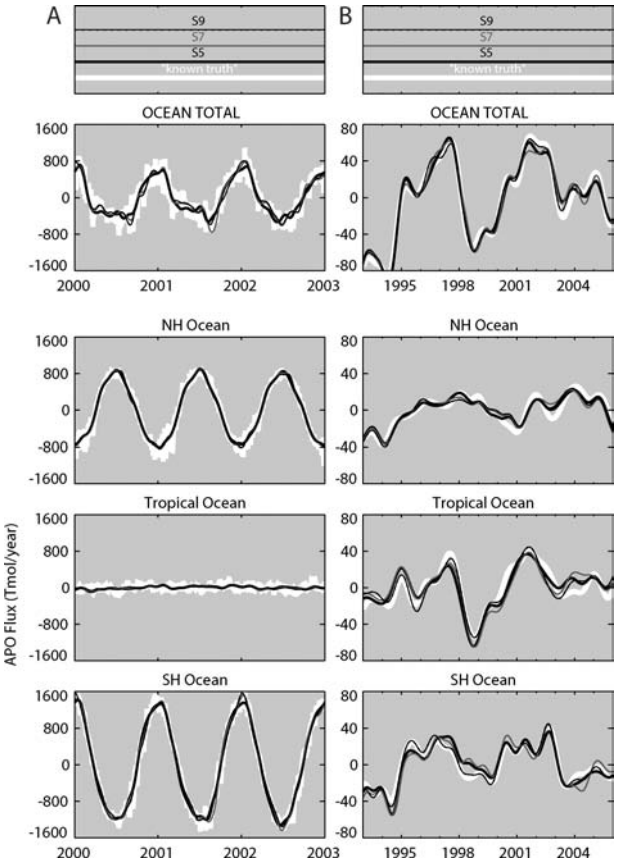

Fig. 11. Capability of the inversion to retrieve a 'known truth' for different sets of observing sites: (A) full variability (three selected years), (B) interannually filtered. Fluxes are integrated over the whole ocean (top row) or three latitude bands (approx. 90° S–20° S, 20° S–20° N, 20° N–90° N; middle and lower rows).

therefore deliberately been excluded from the 'flux model', see Section 2.4.3).

Column B shows the interannual variations (Section 2.5). The IAV of the global APO flux is also reproduced well. The available information further suffices to retrieve the main interannual features in the latitude bands (errors smaller than flux variability). The agreement improves the more sites are used, as expected.

Figure 12 is similar to the IAV column of Fig. 11, but fluxes in each latitudinal band are split into Pacific and Atlantic plus Indian. This longitudinal split seems still to be resolved in the Northern Extratropics and Tropics, somewhat surprising given that there are no observing sites in the Atlantic. The pronounced swing of the 'known truth' in 1997–1998 in the Tropics is correctly located into the Pacific, though some of it is spuriously placed into the Atlantic. In the Southern Extratropics, discrepancies increase, in particular when using five sites only.

For even smaller integration regions, the discrepancies further increase (not shown), indicating that the available information is clearly insufficient to resolve these finer spatial details. In this

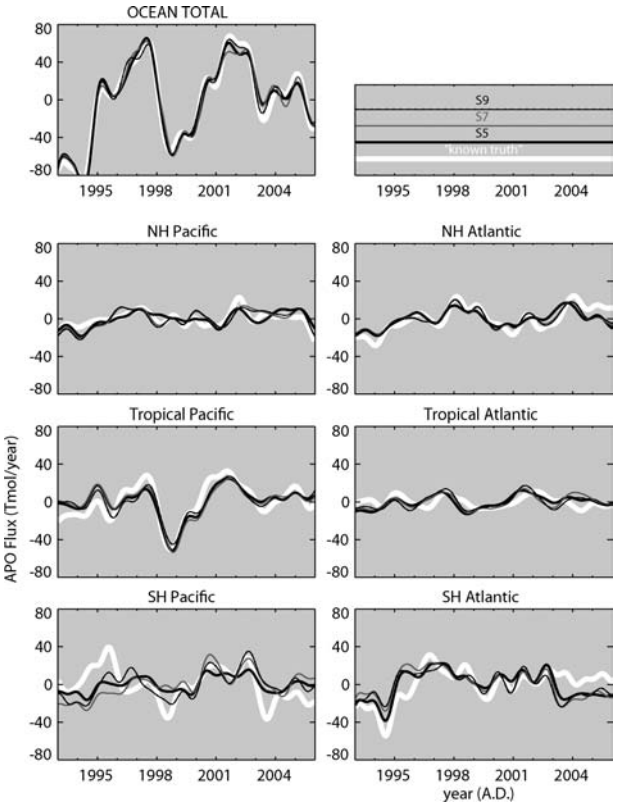

Fig. 12. As Fig. 11 column B, but each latitude band split into a Pacific (left-hand panel) and Atlantic plus Indian (right-hand panel) contribution.

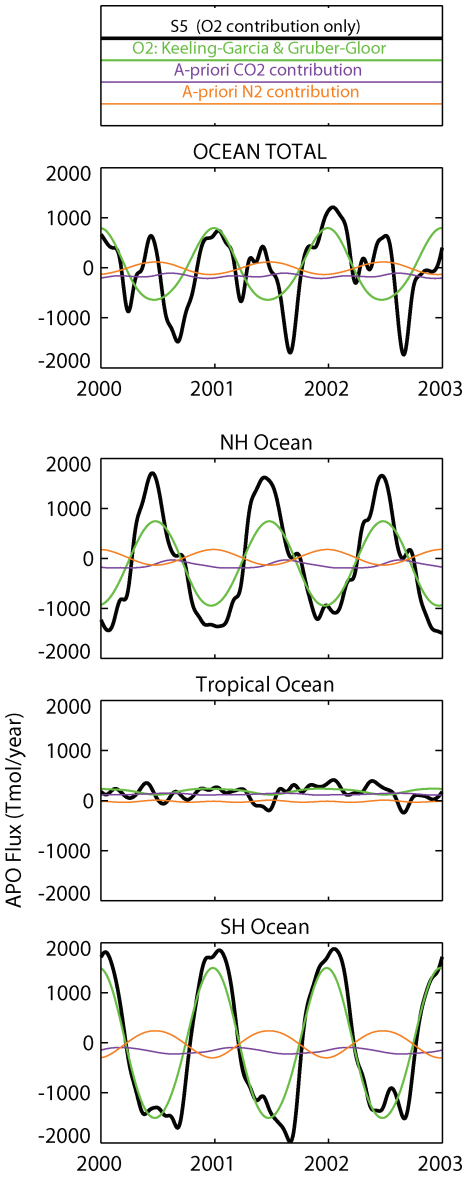

Fig. 13. The APO flux estimates (full variability, selected years, a-priori oceanic CO_2 and N_2 fluxes and fossil-fuel contributions subtracted), compared with an independent O_2 flux climatology (Δp O_2-based O_2 fluxes by Garcia and Keeling, 2001; with long-term values from ocean interior oxygen inversion Gruber et al., 2001). The subtracted a-priori oceanic CO_2 and N_2 contributions to the total APO flux are indicated as thin lines.

paper, therefore, fluxes are mainly shown for the three latitudinal bands as in Fig. 11 only. Essentially the same conclusion regarding the spatial resolution of the inversions is also provided by an examination of the covariance matrix of the a posteriori flux errors (not shown).

Remark. Though the synthetic-data inversions suggest the general suitability of the algorithm, they do not provide a sufficient condition. The real ability to resolve the fluxes is also limited by the various error sources considered in Section 3.2. Further, the degree of success of synthetic inversions is partly specific to the particular properties of the chosen 'known truth'. This also means that synthetic inversions cannot be used to discriminate between the particular setups discussed in Section 3.2.1

10. Appendix D: Estimated Seasonality of APO Fluxes

Figure 13 shows the full temporal variability of estimated APO fluxes (a-priori CO_2 and N_2 contributions subtracted). The extratropical fluxes are dominated by seasonal cycles with peak-to-peak variations of around 3000 TmolAPO yr^{-1}, opposite in phase, whereas the Tropics do not show any seasonality. Inversion results are compared with the smoothed climatology of sea–air O_2 fluxes, based on measurements of partial pressure difference (ΔpO_2) by Garcia and Keeling (2001). The degree of agreement in the phase of the seasonal cycles, which represent completely independent information, lends credibility to the ability of the inversion method to retrieve information on flux variations (even though seasonal cycles are easier matched

than interannual variations due to their much larger amplitudes and their very similar phasing within each of the hemispheres).

References

Baker, D. F., Law, R. M., Gurney, K. R., Rayner, P., Peylin, P. and co-authors. 2006. Transcom 3 inversion intercomparison: Impact of transport model errors on the interannual variability of regional co2 fluxes, 1988–2003. *Global Biogeochem. Cycles* **20**, GB1002, doi:10.1029/2004GB002439.

Battle, M., Mikaloff Fletcher, S., Bender, M., Keeling, R., Manning, A. and co-authors. 2006. Atmospheric potential oxygen: New observations and their implications for some atmospheric and oceanic models. *Global Biogeochem. Cycles* **20**, GB1010.

Behrenfeld, M. J., O'Malley, R. T., Siegel, D. A., McClain, C. R., Sarmiento, J. L. and co-authors. 2006. Climate-driven trends in contemporary ocean productivity. *Nature* **444**, 752–755.

Bender, M. L., Tans, P. P., Ellis, J. T., Orchardo, J. and Habfast, K. 1994. A high precision isotope ratio mass spectrometry method for measuring the O_2/N_2 ratio of air. *Geochim. Cosmochim. Acta* **58**, 4751–4758.

Bender, M. L., Ho, D. T., Hendricks, M. B., Mika, R., Battle, M. O. and co-authors. 2005. Atmospheric O_2/N_2 changes, 1993-2002: Implications for the partitioning of fossil-fuel CO_2 sequestration. *Global Biogeochem. Cycles* **19**, GB4017, doi:10.1029/2004GB002410.

Bousquet, P., Peylin, P., Ciais, P., Le Quéré, C., Friedlingstein, P. and co-authors. 2000. Regional changes in carbon dioxide fluxes of land and oceans since 1980. *Science* **290**, 1342–1346.

Ebisuzaki, W. 1997. A method to estimate the statistical significance of a correlation when the data are serially correlated. *J. Clim.* **10**, 2147–2153.

Feely, R., Boutin, J., Cosca, C., Dandonneau, Y., Etcheto, J. and co-authors. 2002. Seasonal and interannual variability of CO_2 in the equatorial Pacific

Feely, R. A., Takahashi, T., Wanninkhof, R., McPhaden, M. J., Cosca, C. E. and co-authors. 2006. Decadal variability of the air–sea co2 fluxes in the equatorial pacific ocean. *J. Geophys. Res.* **111**, C08S90. *Deep Sea Res.* **49**, 2443–2469.

Fichefet, T. and Maqueda, M. A. M. 1999. Modelling the influence of snow accumulation and snow-ice formation on the seasonal cycle of the Antarctic sea-ice cover. *Clim. Dyn.* **15**, 251–268.

Garcia, H. E. and Keeling, R. F. 2001. On the global oxygen anomaly and air-sea flux. *J. Geophys. Res.* **106**, 31155–31166.

Gaspar, P., Gregoris, Y. and Lefevre, J. M. 1990. A simple eddy kinetic energy model for simulations of the oceanic vertical mixing: tests at station Papa and Long-Term Upper Ocean Study Site site. *J. Geophys. Res.* **95**, 16 179–16 193.

Gent, P. R. and McWilliams, J. C. 1990. Isopycnal mixing in ocean circulation models. *J. Phys. Oceanogr.* **20**, 150–155.

Gloor, M., Gruber, N., Sarmiento, J., Sabine, C. L., Feely, R. A. and co-authors. 2003. A first estimate of present and preindustrial air-sea CO_2 flux patterns based on ocean interior carbon measurements and models. *Geophys. Res. Lett.* **30**, 1010, doi:10.1029/2002GL015594.

Gruber, N., Gloor, M., Fan, S.-M. and Sarmiento, J. L. 2001. Air-sea flux of oxygen estimated from bulk data: Implications for the marine and atmospheric oxygen cycles. *Global Biogeochem. Cycles* **15**, 783–803.

Gurney, K. R., Law, R. M., Denning, A. S., Rayner, P. J., Baker, D. and co-authors. 2002. Towards robust regional estimates of CO_2 sources and sinks using atmospheric transport models. *Nature* **415**, 626–630.

Hamme, R. and Keeling, R. F. 2008. Ocean ventilation as a driver of interannual variability in atmospheric potential oxygen. *Tellus* **60B**, DOI:10.1111/j.1600-0889.2008.00376.x.

Hansen, P. 1998, *Rank-Deficient and Discrete Ill-Posed Problems. Numerical Aspects of Linear Inversion*, Society for Industrial and Applied Mathematics, Philadelphia, USA .

Heimann, M. and Körner, S. 2003. The global atmospheric tracer model TM3, Technical Report 5, Max Planck Institute for Biogeochemistry, Jena, Germany.

Kalnay, E., Kanamitsu, M., Kistler, R., Collins, W., Deaven, D. and co-authors. 1996. The NCEP/NCAR 40-year reanalysis project. *Bull. Am. Met. Soc.* **77**, 437–471.

Keeling, R. F. 1988. *Development of an Interferometric Oxygen Analyzer for Precise Measurement of the Aimospheric O_2 mole Fraction*, Ph.D. thesis, Harvard Univ., Cambridge, USA.

Keeling, R. F. and Shertz, S. R. 1992. Seasonal and interannual variations in atmospheric oxygen and implications for the global carbon cycle. *Nature* **358**, 723–727.

Keeling, R. F., Najjar, R. P., Bender, M. L. and Tans, P. P. 1993. What atmospheric oxygen measurements can tell us about the global carbon-cycle. *Global Biogeochem. Cycles* pp. 37–67.

Keeling, R. F. and Severinghaus, J. P. 2000. Atmospheric oxygen and the carbon cycle. In: *The Carbon Cycle* Volume 6: (eds T. M. L., Wigley and D. S., Schimel), Global Change Institute : Cambridge , Cambridge University Press, pp. 134–140.

Keeling, R. F., Manning, A. C., Paplawsky, W. J. and Cox, A. C. 2007. On the long-term stability of reference gases for atmospheric O_2/N_2 and CO_2 measurements. *Tellus* **59B**, 3–14.

Langenfelds, R., Francey, R. J., Steele, L. P., Battle, M., Keeling, R. F. and co-authors 1999. Partitioning of the global fossil CO_2 sink using a 19-year trend in atmospheric O_2. *Geophys. Res. Lett.* **26**, 1897–1900.

Laws, E. A., Falkowski, P. G., Smith W. O. Jr., Ducklow, H. and McCarthy, J. J. 2000. Temperature effects on export production in the open ocean. *Global Biogeochemical Cycles* **14**, 1231–1246.

Le Quéré, C., Harrison, S. P., Prentice, I. C., Buitenhuis, E. T., Aumont, O. and co-authors. 2005. Ecosystem dynamics based on plankton functional types for global ocean biogeochemistry models. *Global Biogeochem. Cycles* **11**, 2016–2040.

Le Quéré, C., Rödenbeck, C., Buitenhuis, E. T., Conway, T. J., Langenfelds, R. and co-authors. 2007. Saturation of the Southern ocean CO_2 sink due to recent climate change. *Science* **316**, 1735–1738.

Manning, A. C. and Keeling, R. F. 2006. Global oceanic and land biotic carbon sinks from the scripps atmospheric oxygen flask sampling network. *Tellus* **58B**, 95–116.

McKinley, G. A., Follows, M. J. and Marshall, J. 2000. Interannual variability of the air-sea flux of oxygen in the north Atlantic. *Geophys. Res. Lett.* **27**, 2933–2936.

McKinley, G. A., Takahashi, T., Buitenhuis, E., Chai, F., Christian, J. and co-authors. 2006. North Pacific carbon cycle response to climate variability on seasonal to decadal timescales. *J. Geophys. Res.* **111**, doi:10.1029/2005JC003173.

Najjar, R. G. and Keeling, R. F. 2000. Mean annual cycle of the air-sea oxygen flux: a global view. *Global Biogeochemical Cycles* **14**, 573–584.

Nägler, T., Ciais, P., Orr, J., Aumont, O. and Rödenbeck, C. 2007. On evaluating ocean models with atmospheric potential oxygen. *Tellus* **59B**, 138–156.

Olivier, J. G. J. and Berdowski, J. J. M. 2001. Global emissions sources and sinks. In: *The Climate System* (eds. J. Berdowski, R. Guicherit and B. J. Heij), A. A. Balkema Publishers/Swets & Zeitlinger Publishers, Lisse, The Netherlands, 33–78, ISBN 90 5809 255 0.

Peylin, P., Bousquet, P., Le Quéré, C., Sitch, S., Friedlingstein, P., and co-authors. 2005. Multiple constraints on regional CO_2 flux variations over land and oceans. *Global Biogeochem. Cycles* **19**, doi:10.1029/2003GB002214.

Rayner, P., Enting, I., Francey, R. and Langenfelds, R. 1999. Reconstructing the recent carbon cycle from atmospheric CO_2, $\delta^{13}CO_2$ and O_2/N_2 observations. *Tellus* **51B**, 213–232.

Rödenbeck, C., Houweling, S., Gloor, M. and Heimann, M. 2003. CO_2 flux history 1982-2001 inferred from atmospheric data using a global inversion of atmospheric transport. *Atmos. Chem. Phys.* **3**, 1919–1964.

Rödenbeck, C. 2005. Estimating CO_2 sources and sinks from atmospheric mixing ratio measurements using a global inversion of atmospheric transport, Technical Report 6, Max Planck Institute for Biogeochemistry, Jena, Germany.

Schuster, U. and Watson, A. J. 2007. A variable and decreasing sink for atmospheric CO_2 in the North Atlantic. *J. Geophys. Res.* **112**, doi:10.1029/2006JC003941.

Severinghaus, J. P. 1995. *Studies of the Terrestrial O_2 and Carbon Cycles in Sand due to Cases and in Biosphere 2*, Ph.D. thesis, Columbia Univ., New York, USA .

Stephens, B. B., Keeling, R. F., Heimann, M., Six, K. D., Murnane, R. and co-authors. 1998. Testing global ocean carbon cycle models using measurements of atmospheric O_2 and CO_2 concentration. *Global Biogeochem. Cycles* **12**, 213–230.

Stephens, B. B., Bakwin, P. S., Tans, P. P., Teclaw, R. M. and Baumann, D. D. 2007. Application of a differential fuel-cell analyzer for measuring atmospheric oxygen variations. *J. Atmos. Ocean. Technol.* **24**, 82–94.

Takahashi, T., Sutherland, S. C., Sweeney, C., Poisson, A. and co-authors. 2002. Global sea-air CO_2 flux based on climatological surface ocean pCO_2, and seasonal biological and temperature effects. *Deep Sea Res. II* **49**, 1601–1623.

Tohjima, Y., Mukai, H., Machida, T. and Nojiri, Y. 2003. Gas-chromatographic measurements of the atmospheric oxygen/nitrogen ratio at hateruma island and cape ochi-ishi, japan. *Geophys. Res. Lett.* **30**, 1653, doi:10.1029/2003GL017282.

Tohjima, Y., Mukai, H., Machida, T., Nojiri, Y. and Gloor, M. 2005. First measurements of the latitudinal atmospheric O_2 and CO_2 distributions across the western pacific. *Geophys. Res. Lett.* **32**, L17805.

Weiss, R. F. 1970. The solubility of nitrogen, oxygen and argon in water and seawater. *Deep-Sea Res.* **17**, 721–735.